remote sensing

Article

Sustainable Monitoring of Mining Activities: Decision-Making Model Using Spectral Indexes

Krystyna Michałowska [1,2], Tomasz Pirowski [1,2], Ewa Głowienka [1,2,*], Bartłomiej Szypuła [3,4] and Eva Savina Malinverni [5]

1 Department of Photogrammetry, Remote Sensing, and Spatial Engineering, Faculty of Geo-Data Science, Geodesy, and Environmental Engineering, AGH University of Krakow, 30-059 Krakow, Poland; michalowska@agh.edu.pl (K.M.); pirowski@agh.edu.pl (T.P.)
2 Department of Land Surveying, Faculty of Environmental Engineering and Land Surveying, University of Agriculture in Krakow, 31-120 Krakow, Poland
3 Institute of Earth Sciences, Faculty of Natural Sciences, University of Silesia in Katowice, 40-007 Katowice, Poland; bartlomiej.szypula@us.edu.pl
4 Śląskie Laboratorium GIS (ŚLabGIS), Centre for Polar Studies, University of Silesia in Katowice, 40-007 Katowice, Poland
5 Department of Civil, Building and Architecture, Marche Polytechnic University, 60121 Ancona, Italy; e.s.malinverni@staff.univpm.it
* Correspondence: eglo@agh.edu.pl

Abstract: In response to the escalating demand for mineral resources and the imperative for sustainable management of natural assets, the development of effective methods for monitoring mining excavations is essential. This study presents an innovative decision-making model that employs a suite of spectral indices for the sustainable monitoring of mining activities. The integration of the Combinational Build-up Index (CBI) with additional spectral indices such as BRBA and BAEI, alongside multitemporal analysis, enhances the detection and differentiation of mining areas, ensuring greater stability and reliability of results, particularly when applied to single datasets from the Sentinel-2 satellite. The research indicates that the average accuracy of excavation detection (overall accuracy, OA) for all test fields and data is approximately 72–74%, varying with the method employed. Utilizing a single CBI index often results in a significant overestimation of producer's accuracy (PA) over user's accuracy (UA), by about 10–14%. Conversely, the introduction of a set of three complementary indices achieves a balance between PA and UA, with discrepancies of approximately 1–3%, and narrows the range of result variations across different datasets. Furthermore, the study underscores the limitations of employing average threshold values for excavation monitoring and suggests the adoption of dedicated monthly thresholds to diminish accuracy variability. These findings could have considerable implications for the advancement of autonomous and largely automated systems for the surveillance of illegal mining excavations, providing a predictable and reliable methodology for remote sensing applications in environmental monitoring.

Keywords: Sentinel-2; spectral indexes; mining excavation detection; sustainable monitoring; multitemporal analysis

Citation: Michałowska, K.; Pirowski, T.; Głowienka, E.; Szypuła, B.; Malinverni, E.S. Sustainable Monitoring of Mining Activities: Decision-Making Model Using Spectral Indexes. *Remote Sens.* **2024**, *16*, 388. https://doi.org/10.3390/rs16020388

Academic Editor: Dimitrios A. Georgakellos

Received: 9 November 2023
Revised: 29 December 2023
Accepted: 10 January 2024
Published: 18 January 2024

1. Introduction

Every type of mining activity should be conducted in accordance with the mining and geological law applicable in a given country. Unfortunately, numerous abuses still occur. Such actions are harmful to mineral deposits and the natural environment, but they are also dangerous for workers involved in illegal mining and pose a threat to public safety. In Poland, between 2015 and 2022, 2627 reports of illegal exploitation were made, for which penalties totaling nearly 43 million US dollars were imposed [1].

The aim of this research is to develop a method for detecting illegal mining sites and open-pit mines located on the Earth's surface. The use of publicly available multispectral satellite images allows for advanced remote analysis, which will enable a quick assessment of the scale of rock raw material extraction in the indicated areas. This approach is much cheaper, faster, and more convenient compared to traditional ground measurements.

The burgeoning interest in monitoring illegal mining activities through remote sensing is a response to the escalating environmental and socio-economic impacts these activities have globally. Illegal mining poses significant threats to ecological balance, often leading to deforestation, soil degradation, and water contamination. Recent global studies, such as those by [2,3], have highlighted these adverse effects and underscored the need for effective monitoring mechanisms, Camalan et al. [4] provide a comprehensive overview of the environmental repercussions of unregulated mining in various ecosystems, emphasizing the role of advanced remote sensing techniques in mitigating these impacts. Lobo et al. [5], on the other hand, delve into the socio-economic aspects, illustrating how illegal mining fuels conflicts and undermines local economies.

In the conducted research, the concept of using spectral indices for reliably distinguishing excavation areas was adopted. Remote sensing differentiation of excavations is a challenging issue, as they are characterized by a similar or almost identical spectral response compared to exposed soils, which in turn show many spectral features common to buildings. Therefore, the first step was to review the literature on existing spectral indices dedicated to exposed soils, buildings, and minerals, assuming that they will be potentially the best indicators for the research objective.

In the context of the escalating global crises of climate change and environmental degradation, the sustainable management of natural resources has become a paramount concern. The mining sector, as a significant contributor to these challenges, is in urgent need of innovative approaches to ensure that its activities are conducted responsibly. This study contributes to this need by presenting a novel method for the detection of illegal mining activities, which are often overlooked yet have substantial impacts on the environment. By leveraging the capabilities of multispectral satellite imagery, this research aligns with the principles of sustainable production, offering a tool for the energy sector to monitor and regulate mining operations more effectively.

Indices have been formulated since the 1980s, using only the four available bands of the Landsat satellite (B, G, R, NIR), initially mainly related to biomass. Already then, the first proposals for indices taking into account the influence of the soil background appeared [2,3,6,7] as well as for detecting minerals [8]. With the increase in the number of bands (especially covering the mid-infrared), indices related to detecting soils and/or buildings were defined. In this first group, dedicated to the detection of exposed soils, there were indices such as BSI [9,10], BCI [11], RNDSI [12], MNDBI [13], and MBI [14] (details regarding equations as well as expanded acronyms to full names are explained further in the text). In this group, primarily the differences in spectral reflectance noted between the medium infrared SWIR2 and the visible channels are utilized. This is due to the high reflectivity of exposed soils in the SWIR2 channel, with a decrease in spectral reflection in this band for other classes. In the spectral indices (BSI, BSI_1, MBI), combinations of SWIR2 with other infrared channels (SWIR1 and NIR) and/or results of the Tasseled Cap transformation (BCI, RNDSI) are additionally taken into account. Intermediate features were also used to detect exposed soils, for example, by defining indicators in terms of shadow (ShDI [14]) or biomass (TCWVI [14], NDVI-GREEN [15]) or dry lands DBSI [16]). Similarly, numerous equations were defined for detecting buildings: UI [17], NDTI [18], BU [19], NDBI [9,19], 3BUI [20], BAEI [21], CBI [22], BRBA [23], NBAI_B [23], RUI and NRUI [24], BLEIF [25], and NBAI_G [26]. This group of indices is more diverse, depending on the analysis terrain, and it uses only differences in reflection noted between infrared channels (UI, NDTI, NDBI), and combinations of—three or four—infrared and visible channels (NBAI_B, NBAI_G, BLEIF), including in the unnormalized scale (3BUI, BAEI). Many of the equations combine the action of other, basic indices (RUI, NRUI, CBI, BU), to even more strongly utilize differences accentuated by the basic indices between the classes of buildings, vegetation, and exposed soils. The large number of proposed spectral indices, having names like “urbanized zones” and “built-up”, in practice also serve as indices for detecting soils, because—as mentioned earlier—the main problem in optical detection, especially in dry zones, is the correct separation of soils from buildings. Therefore, some of the indices related to detecting and differentiating soils and buildings are based on detecting impermeable surfaces, such as NDSI [27] or PISI [26] or determining the shares of built-up and vegetation pixels (VIBI [28]) or built-up and unbuilt lands (BBI [29]). Some building and soil indices, developed for Landsat 8, are built using thermal channels, for example, NDBaI [30], NDSI [31], EBBI [32], BAEM [33], NBLI [34], and DBI [16], assuming the use of heating up of artificial zones is faster than that of natural ones.

The use of indices varies: from relatively simple solutions based on thresholding and quantization of indices, including often new, original equations (e.g., [14,16,25,32,35]), through to combinations of such operations [19,31,36] or the use of logical conditions between index values [31], multi-indicator models [37–39], or the building of new indicators based on existing indicators or results of linear image transformations [13,24,26,28], ending with automatic procedures on spectral channels, but supplemented with spectral indices [23,31,40–42].

From the literature review, it appears that spectral indices are most often used to distinguish city boundaries from agricultural areas. Often these are dry, even semi-desert areas, where the difficulty in distinguishing built-up areas from exposed soils and sparsely vegetated areas, which are relatively common due to difficult climatic conditions, increases. Only a few works concern the monitoring or detection of building materials occurring on the surface, such as gravels, sands, or rock material in quarries. An example of a study using the current capabilities of remote sensing imaging for detailed differentiation of minerals, detectable thanks to rock outcrops, is the work of Sekandari et al. [42]. Tests were conducted for northern Iran, based on Landsat, Sentinel-2, and World-View data. Spectral indices and PCA transformation were used in the research. Band combinations, calculated using the weighting of the red and blue bands and SWIR1/SWIR2, allowed iron oxides and hydroxides to be distinguished from clay and carbonate minerals.

Another example of mapping construction materials—sandbanks and river gravel—is the publication by Stančič et al. [43]. Using data from Landsat 8 and Sentinel-2, the authors monitored the Soča river area in Slovenia. For mapping, they applied the classification methods SAM (Spectral Angle Mapper) [44] and fuzzy SSMA (Spectral Signal Mixture Analysis) (Unmixing) [43], additionally introducing indices MNDWI, NDWI, NDVI, NDII, and NDVI-GREEN to the classification algorithm. A study closely related in theme to the conducted research is the article by Usmanov et al. [45], concerning the detection of illegal extraction sites of non-metallic minerals, such as sand pits, clay, carbonate rocks, and gravel. The authors, focusing on the Tatarstan region and using Sentinel-2 data, employed several spectral indices, mainly dedicated to soils but also vegetation (NDVI, R82, NDSI, DBSI, SMI, IRI_SWIR1, CI, SRCI, BI, NDBI, SAVI, BSI). Using supervised classification, 10 available channels, and 12 spectral indices, they selected the most effective combination of input data. Their experiments showed that for detecting and distinguishing quarries, the simultaneous use of two or more indices yields slightly better results than using spectral channels alone. For sands, these were the CI and NDSI indices and the RED channel; for gravel, the CI index and the BLUE and RED channels; for clay, the NDVI and NDSI indices and the RED and SWIR1 channels; and for carbonate rocks, the SMI index and three visible channels.

Summarizing the literature review, it is worth noting the following:

(1) A large number of diverse spectral indices have been formulated, of which those dedicated to buildings and soils are most useful for the research purpose set here, while in many cases, plant indices also play a significant role; the experiences reported in publications mainly concern the separation of major types of land cover, i.e., soil versus buildings, and secondly, they characterize rock outcrops or soil subtypes;
(2) Despite the large number of developed indices and their documented usefulness, new equations are still being built, even in the latest literature (e.g., [13,14,16,24,25,35]). This is because, when analyzing specific areas for a specific purpose using specific

satellite data, it is possible to achieve higher recognition efficiency thanks to new indices tailored/created for specific needs;

(3) The methodology of using spectral indices is very diverse, and it is impossible to indicate solutions that are clearly better or universal—in selected cases, simple thresholding on indices gave higher accuracies than classification methods with introduced index images (e.g., [13,31]), while in other cases, it is the opposite [25], so there is no possibility to compare their mutual efficiency (e.g., [14,16,36,40,41]);

(4) In many studies, the adopted method of selecting threshold values could have influenced the results obtained—there were methods of their manual setting, statistical (like Otsu or using unsupervised classifiers), ending with logical or graphical conditions used for multi-index methods; only a few publications tested the impact of the way thresholds are set on the final result [16,26];

(5) Despite many years of experience, no uniform procedures have been developed, even related to preliminary image processing; although, in most literature examples, data are subjected to radiometric corrections (such as removing the influence of the atmosphere, operating albedo values instead of DN, using higher levels of satellite image processing, available mainly for new data sources such as Sentinel-2 or Landsat 8), this is not the rule;

(6) No uniform criteria for evaluating the performance of the methods and indices used have been formulated; most often, accuracies are given for specific, sought-after types of land cover classes—various accuracy measures are used here, such as PA (producer's accuracy), UA (user's accuracy, reliability), and kappa—without specifying the confidence level of the results, without specifying the selection strategy, and sometimes even without the number of verification points [13,31,32,41,43], and there are also many evaluations based only on photo-interpretation analysis (e.g., [23,41]); there have been few attempts to show the differences in the operation of indices, for example, by comparing the consistency of their operation [35], as a graphical diagram [28], by using spectral separation measures [24] or studying the consistency of PA and UA [10].

Based on the above, generalized conclusions, at this stage of the research, it was decided to subject all the above-mentioned spectral indices of soil/building to uniform tests, which can be directly applied or adapted for Sentinel-2 bands. This approach allowed for an objective assessment of the efficiency of the indices, especially for the basic, atypical purpose, which is the additional distinction of excavations from exposed soils. The adopted scope of research focused on specific conditions occurring in southern Poland. In the assumed scope of research, the indices were used individually or complementarily through specific decision and logical schemes—in both cases based on uniformly adopted optimization of threshold values.

In summary, our research aims to develop an innovative method for the detection of illegal mining sites and open-pit mines using multispectral satellite images, primarily focusing on spectral indices. Our approach involves a meticulous examination of various spectral indices, particularly those related to soils, buildings, and minerals, to distinguish excavation areas from exposed soils and buildings, a challenging task due to their similar spectral responses. We integrate the use of Sentinel-2 datasets, leveraging their rich spectral information for precise and sustainable monitoring. Through this method, we intend to contribute significantly to the field of remote sensing in environmental monitoring, especially in the sustainable management of mining activities. Our study's unique aspect lies in its application of a diverse set of spectral indices, optimized thresholding techniques, and a methodological framework structured in distinct phases to ensure the comprehensive analysis and reliable detection of mining activities.

Furthermore, the proposed method supports the goals of environmentally responsible consumption by providing a means to enforce compliance with mining regulations, thereby ensuring that the minerals entering the supply chain are sourced sustainably. This is particularly relevant in light of the increasing demand for minerals that are critical for green technologies, such as those used in renewable energy systems. The ability to monitor mining activities remotely not only aids in the protection of the environment but also promotes transparency and accountability within the supply chain.

2. Study Area and Source Data

2.1. Study Area

In the current research phase, three test areas (I, II, III) were identified in the south of Poland, where diverse mineral deposits are available for exploitation (Figure 1). Each of the areas exhibits distinct physiogeographic conditions, primarily influenced by the terrain and geology, as well as by land use patterns. Within the physiogeographic regionalization of Poland, two of the areas fall within the Polish Uplands belt: test field I in the Silesia-Kraków Upland and test field II in the Małopolska Upland. In contrast, test field III is situated in the Sandomierz Basin [46,47].

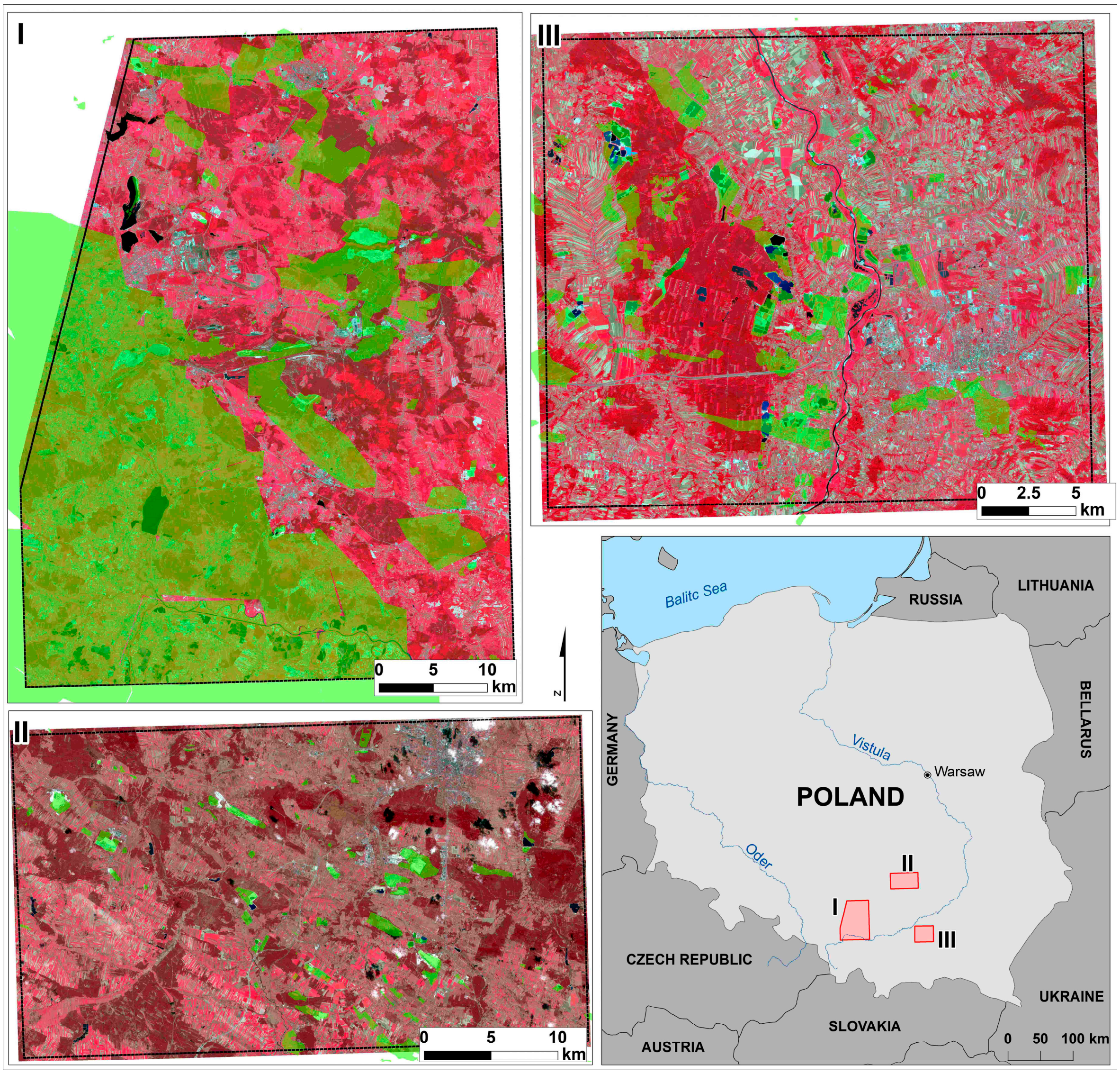

Figure 1. Location and extent of the study areas: Areas I, II, and III, with the mineral deposits highlighted in green. Background image © EU-Sentinel. False-color composite infrared (FCC CIR) image using Sentinel-2 satellite bands B08 (near-infrared), B04 (red), and B03 (green). L2A_T34UCA_A011788_20190609T094208 (**I**). L2A_T34UDB_A011831_20190612T095109 (**II**). L2A_T34UDA_A012503_20190729T094242 (**III**).

The first test field (I) covers the largest area, spanning over 2400 km^2. This region boasts a highly diverse topography: from the Vistula River valley in the south to the limestone and dolomite outcrops in the east and north. The topographical range reaches nearly 280 m. This area contains backfilling and foundry sands, natural aggregates, building ceramic raw materials, limestones, dimension and crushed stones, as well as zinc and lead ores. The next test field (II) occupies just over 1000 km^2. It is also a region with significant elevation differences: from the Nida River valley in the south to the sandstone, limestone, and dolomite ridges in the central and northern parts of the area. The local relief is almost 200 m. This area is rich in limestones and marls for the lime and cement industry, natural aggregates, and dimension and crushed stones. The last area (III) is the smallest, covering 705 km^2, and is the least morphologically diverse—it is dominated by the broad, flattened valley of the Dunajec River, with the highest loess-covered elevations located in the south. This region is abundant in natural aggregates, building ceramic raw materials, and rock salt.

Drawing from the 2018 Corine Land Cover database [48], we categorized the land into four primary classes: artificial surfaces (111–142), agricultural areas (211–243), forest and semi-natural areas (311–333), and wetlands and water bodies (411–512). Despite the pronounced spatial diversity in land cover across the selected research areas, the proportional distribution among these classes remains notably consistent. The agricultural areas class is predominant, ranging from 39% in test field I to 61% in test field II. This is closely followed by the forest and semi-natural areas class, which varies from 21% in test field III to 37% in test field I. Artificial surfaces account for a slightly smaller portion, with its presence fluctuating between 15% in test field II and 20% in test field I. In each area—regardless of its geographical location and topography—the wetlands and water bodies occupy the smallest area (ranging from 0% to 2.5%), while mineral extraction sites cover an average of 1.5% of the area.

2.2. Source Data

Multi-temporal Sentinel-2 datasets from 2019 were obtained for each designated test area. The selection of the year for scene acquisition was guided by the availability of corresponding reference data, predominantly the Corine Land Cover database from 2018. The criteria for image selection included: a timeframe from April to September, a cloud cover of less than 5%, a data processing level of L2A, and the requirement that test areas be encompassed within a single scene (thus avoiding the need for mosaicking). The initial plan was to acquire imagery at approximately monthly intervals, targeting six images per test field. In practice, due to cloud cover, this criterion was not always met, and data gaps were permitted, particularly on the peripheral segments of test field I (notably the northwest corner of the scene). The image datasets that satisfied the selection criteria and were subsequently utilized in the analysis are detailed in Table 1.

At various stages of the test work, the ability to efficiently use multispectral imagery as a base for visual interpretation is crucial. Based on experience and the analysis of color composition informational potential indicators (maximum orthogonal complement information, MOCI; optimum index factor, OIF), a complementary set of color compositions was adopted, consisting of four composites (Sentinel-2 channels in RGB display order): B02-B03-B04 (denoted as CC TC), B03-B04-B08 (FCC CIR), B03-B11-B08 (FCC 3-11-8), B03-B08-B12 (FCC 3-8-12). All Sentinel-2 A, B satellite scenes were downloaded from the European Space Agency [49] service using the Semi-Automatic Classification Plugin in the QGIS software platform [50].

Data on mineral resources found in Poland were obtained from the MIDAS database of the Polish Geological Institute [51].

Table 1. Characteristics of satellite data used in the analyses.

Study Site (Test Fields)	Date	Repository, Data Acquisition; Orthophoto, Level L2A. WGS84/UTM EPSG: 32638
I	18 April 2019 19 June 2019 26 August 2019 22 September 2019	L2A_T34UCA_A019953_20190418T095032 L2A_T34UCA_A011788_20190609T094208 L2A_T34UCA_A021812_20190826T095031 L2A_T34UCA_A022198_20190922T094031
II	15 April 2019 12 June 2019.06.12 29 July 2019.07.29 28 August 2019 22 September 2019	L2A_T34UDB_A019910_20190415T094033 L2A_T34UDB_A011831_20190612T095109 L2A_T34UDB_A012503_20190729T094242 L2A_T34UDB_A012932_20190828T094520 L2A_T34UDB_A022198_20190922T094031
III	5 April 2019 29 July 2019 28 August 2019 22 September 2019	L2A_T34UDA_A019767_20190405T094119 L2A_T34UDA_A012503_20190729T094242 L2A_T34UDA_A012932_20190828T094520 L2A_T34UDA_A022198_20190922T094031
Satellite characteristics: Sentinel-2A, Sentinel-2B, band/central wavelength		
Multispectral Bands (MS); spatial resolution 10 m; Blue B02: 0.492/0.492; Green B03: 0.560/0.559; Red B04: 0.665/0.665; NIR B08: 0.833/0.833 Multispectral Bands (MS); spatial resolution: 20 m; RedEdge B05: 0.704/0.704 RedEdge B06: 0.740/0.740 RedEdge B07: 0.783/0.780 Narrow NIR1 B8A: 0.865/0.864 SWIR1 B11: 1.614/1.610 SWIR2 B12: 2.202/2.186 Multispectral Bands (MS); spatial resolution: 60 m Coastal aerosol B01: 0.443/0.442 Water vapor B09: 0.945/0.943 SWIR Cirrus B10: 1.373/1.378		
Color composites to enhance the photointerpretation properties (for each area, at each registration date)		
Color Composites: True Color (CC TC); Bands B-G-R; B02-B03-B04 Color Composites: False Color (FCC CIR); Bands G-B-NIR; B03-B04-B08 Color Composites: False Color (FCC 1); Bands G-NIR-SWIR2; B03-B08-B12 Color Composites: False Color (FCC 2); Bands R-SWIR1-NIR; B04-B11-B08		

3. Methods

The methodology employed in this study is structured into six distinct phases, each building upon the previous to ensure a comprehensive analysis. These phases are delineated and visually summarized in Figure 2.

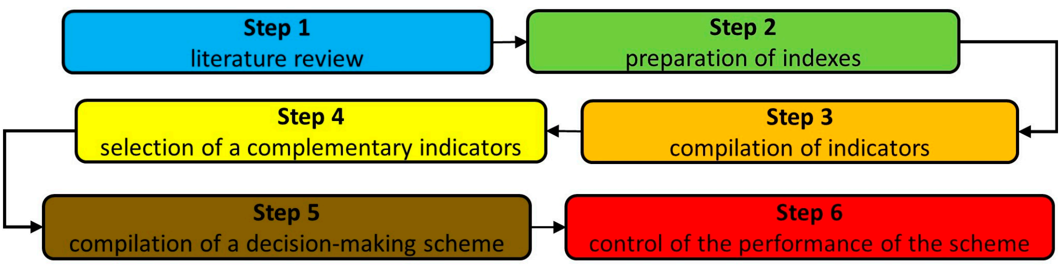

Figure 2. Schematic representation of the workflow detailing the six main stages of the research methodology.

In Table 2, spectral indices for 34 indices prepared for application with Sentinel-2 bands are compiled. Indices that utilize thermal data and panchromatic imagery were omitted. Indices that are repeated under different names were used once (such as NDSI, NDBI, NDII). In ambiguous cases, when a medium infrared (MIR/SWIR) channel appears in the spectral index, the assignment of the MIR/SWIR channel to SWIR1 (Sentinel-2, B11) or SWIR2 (Sentinel-2, B12) was determined based on the source publications, by reading the band characteristics used in the studies of individual authors (this was performed, for example, for indices like NDII, NBI).

Table 2. Schematic representation of the workflow detailing the six main stages of the research methodology.

No.	Index Name	Adopted Equations for Sentinel-2	SDI exc-soi *	SDI exc-bui *
1	3BUI (BI) Three-band Urban Index (Barren Index)	$B04 + B11 - B08$	0.74	1.38
2	BAEI Built-up Area Extraction Index	$\frac{B04 + 0.3}{B03 + B11}$	0.64	1.08
3	BBI Built-up and Bare Land Index	$\left(\frac{B02 - B03}{B02 + B03}\right) + \left(\frac{B04 - B03}{B04 + B03}\right)$	0.62	0.65
4	BCI Biophysical Composition Index	$\frac{\left(\frac{TC1 + TC3}{2} - TC2\right)}{\left(\frac{TC1 + TC3}{2} + TC2\right)}$ (TC1, TC2, TC3—transf. Tasseled Cap)	0.21	0.28
5	BI_Br Brightness Index	$\sqrt{B04^2 + B08^2}$	0.97	0.98
6	BLFEI Built-up Land Features Extraction Index	$\frac{\left(\frac{B03 + B04 + B12}{3} - B11\right)}{\left(\frac{B03 + B04 + B12}{3} + B11\right)}$	1.26	0.15
7	BRBA Band Ratio for Built-up Area	$\frac{B03}{B08}$	1.53	0.27
8	BSI Bare Soil Index	$\frac{(B12 + B04) - (B08 - B02)}{(B12 + B04) + (B08 + B02)}$	0.76	0.48
9	BSI_1 Bare Soil Index 1	$\frac{(B12 + B04) - (B08 + B02)}{(B12 + B04) + (B08 + B02)}$	1.00	0.28
10	BU Built-up Index	NDBI—NDVI	0.01	0.35
11	CBI Combinational Build-up Index	$\frac{\left(\frac{PC1 + NDWI}{2} - SAVI\right)}{\left(\frac{PC1 + NDWI}{2} + SAVI\right)}$ $NDWI = \frac{B03 - B08}{B03 + B08}$ $SAVI = \frac{(B08 - B04)}{(B08 + B04 + 0.5)} \times 1.5$ PC1, NDWI, SAVI—norm. to 0–1	1.32	1.06
12	CI Crust Index	$1 - \frac{B04 - B02}{B04 + B02}$	1.21	0.32
13	DBSI Dry Bareness Index	$\frac{B11 - B03}{B11 + B03} - NDVI$	1.05	0.07
14	IBI Index-based Built-up Index	$\frac{\frac{2B11}{B11 + B08} - \left[\frac{B08}{B08 + B04} + \frac{B03}{B03 + B11}\right]}{\frac{2B11}{B11 + B08} + \left[\frac{B08}{B08 + B04} + \frac{B03}{B03 + B11}\right]}$	0.83	0.12
15	IRI_SWIR1 InfraRed Index-Short Wave InfraRed 1	$\sqrt{\frac{B08^2 + B12^2}{B11}}$	0.90	1.07

Table 2. *Cont.*

No.	Index Name	Adopted Equations for Sentinel-2	SDI exc-soi *	SDI exc-bui *
16	MBI Modified Bare Soil Index	$\frac{B11 - B12 - B08}{B11 + B12 + B08} + 0.5$	0.82	0.08
17	MNDBI Modified Normalized Difference Bare-land Index	$\frac{B12 - B02}{B12 + B02}$	1.27	0.25
18	NBAI_B Normalized Built-Up Area Index (Blue)	$\frac{B12 - \frac{B08}{B02}}{B12 + \frac{B08}{B02}}$	1.20	1.02
19	NBAI_G Normalized Built-Up Area Index (Green)	$\frac{B12 - \frac{B11}{B03}}{B12 + \frac{B11}{B03}}$	1.40	0.99
20	NBI New Built-up Index	$\frac{B04 \times B11}{B08}$	0.90	1.34
21	NDSI_1a/NDBI Normalized Difference Soil Index/Normalized Difference Built-up Index	$\frac{B11 - B08}{B11 + B08}$	0.65	0.13
22	NDTI Normalized Difference Tillage Index	$\frac{B11 - B12}{B11 + B12}$	0.51	0.60
23	NDVI-GREEN Normalized Difference Vegetation Index—Green	$B03 \times \frac{B08 - B04}{B08 + B04} = B03 \times NDVI$	0.00	0.63
24	NRUI Normalized Ratio Urban Index	$\frac{RUI - NDSI_{1a}}{RUI + NDSI_{1a}}$	0.40	0.13
25	PISI Perpendicular Impervious Surface Index	$0.8192 \times B02 - 0.5735 \times B08 + 0.075$	0.71	0.35
26	R82 Ratio B08/B02	$\frac{B08}{B02}$	1.42	0.04
27	RNDSI Ratio Normalized Difference Soil Index	$\frac{\text{Normalized\_NDSI2}}{\text{Normalized\_TC1}}$ $NDSI2 = \frac{B12 - B03}{B12 + B03}$ TC1-soils (high albedo) from transf. Tasseled Cap NDSI2 i TC1—normalized to 0–1	1.12	0.72
28	RUI Ratio Urban Index	$RUI = \frac{BCI}{NDSI_{1a}}$	0.29	0.16
29	ShDI Shadow Index	$\frac{2 \times B08 - B12}{2 \times B08 + B12} - \frac{B08 - B02}{B08 + B02} + 4 \times B04$	1.35	0.70
30	SMI Salt Minerals Index	$\sqrt{\frac{B02^2 + B03^2 + B04^2}{B12}}$	1.39	0.43
31	SRCI Simple Ratio Clay Index	$\frac{B11}{B12}$	0.50	0.59
32	TCWVI A Tasseled Cap Water and Vegetation Index	$\frac{TC1 - TC2}{TC1 + TC2}$ from Tasseled Cap transformation: TC1-gleby (low albedo for water); TC2-vegetation;	1.06	0.28
33	UI Urban Index	$\left[\frac{B12 - B08}{B12 + B08} + 1\right] \times 100$	0.40	0.33
34	VIBI Vegetation Index Built-up Index	$\frac{NDVI}{NDVI + NDBI}$	0.03	0.08

* Meaning of subscripts: exc-soi (excavation—soil), exc-bui (excavation—built-up).

The third test field served as the primary testing ground for the preliminary assessment of the usefulness of spectral indices. Each of the spectral indices listed in Table 2 was calculated using April data from Sentinel-2. At this stage, the usefulness of an index was determined by its ability to spectrally differentiate the main types of land categories. A division into six broadly understood classes was adopted, the first three of which were particularly important for the research objective, namely (1) excavations (open-pit exploitation of gravels, sands, quarries), (2) bare soils (in the area of agricultural lands/cultivations), (3) built-up areas (all artificial lands—areas of compact and scattered development; communication lines, engineering structures, commercial and industrial areas), (4) low vegetation (crops, meadows, pastures, fallow lands), (5) high vegetation (wooded areas, forest lands, urban parks), and (6) surface waters (rivers, lakes, ponds, sedimentation tanks).

For each type of land cover, 340 training points were prepared (Figure 3). Their identification was performed photointerpretatively. Based on experience and the analysis of the informational potential of color compositions (MOIK, OIF), four color compositions were considered complementary for such interpretative work (Sentinel-2 channels in the BGR display order): B02-B03-B04 (designation CC TC), B03-B04-B08 (FCC CIR), B03-B11-B08 (FCC 3-11-8), B03-B08-B12 (FCC 3-8-12).

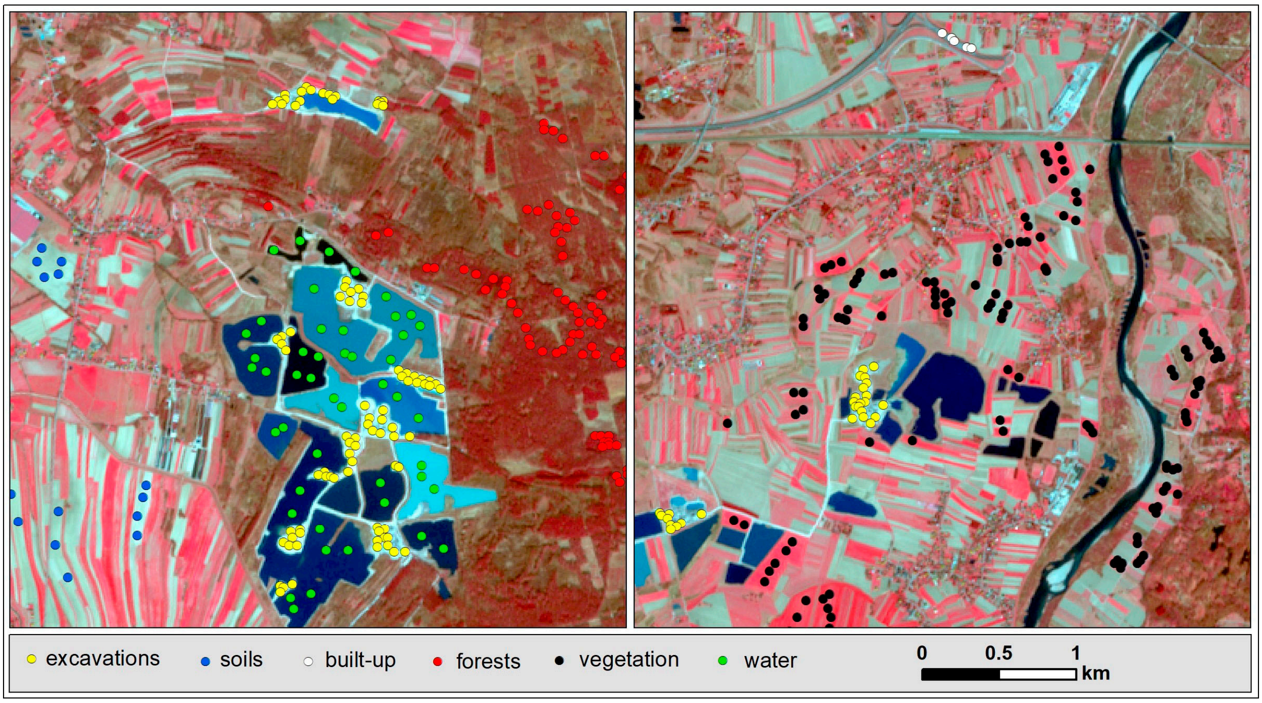

Figure 3. Fragments of Test Field III marked with training points. Background image © EU-Sentinel. Sentinel-2. FCC CIR. 5 April 2019. L2A_T34UDA_A019767_20190405T094119.

In the next step, utilizing the prepared training points, basic statistical parameters such as mean pixel brightness and standard deviations were calculated for each of the six main land cover categories. The potential for class separation was evaluated using the Spectral Discrimination Index (SDI) as described by Radeloff [52] (1).

$$SDI_{a-b} = \frac{|\mu_a - \mu_b|}{\delta_a + \delta_b} \quad (1)$$

SDI is calculated for specified pairs of land cover categories. This measure examines the difference between the mean brightness of class samples, expressed in units of their standard deviations. Therefore, it takes into account both the differences in class brightness, expressed in absolute values, and the variance of the classes under study. This allows for an assessment of the extent to which the spectral characteristics of classes "overlap" on a given image (for example, a spectral channel or spectral index).

Key SDI values for each of the indices are provided in Table 3. The compilation includes only the following combinations of pairs as the classes most spectrally similar:

excavation—bare soil; excavation—built-up area. Vegetation and water masking were performed separately, using dedicated indices for this purpose (see the scheme in Figure 4, and Equations (3) and (4)), and hence, reporting SDI for combinations including these classes was unnecessary.

Table 3. Compilation of sample parameters for classes and adopted threshold values—an example of three spectral indices with the highest SDI values for $SDI_{exc\text{-}soi}$ and $SDI_{exc\text{-}bui}$ in test field III, on 5 April 2019. The threshold values for the CBI index correspond to the curve intersections illustrated in Figure 5.

Index	Category	Mean	SD	−2 SD	+2 SD	Min of the Range	Max of the Range
CBI	excavations	0.138	0.028	0.081	0.195	0.101	0.195
	soils	0.036	0.049	−0.062	0.134	0.018	0.101
	built-up	−0.027	0.127	−0.281	0.227	−0.281	0.018
NBAI_B	excavations	−0.661	0.059	−0.779	−0.543	−0.740	−0.543
	soils	−0.782	0.031	−0.845	−0.719	−0.790	−0.740
	built-up	−0.810	0.083	−0.976	−0.644	−0.976	−0.790
NBAI_G	excavations	−0.651	0.053	−0.756	−0.546	−0.725	−0.546
	soils	−0.778	0.038	−0.853	−0.702	−0.784	−0.725
	built-up	−0.803	0.100	−1.003	−0.602	−1.000	−0.784

The higher the SDI value, the less overlap there is between two classes. It is assumed that an SDI < 1 indicates poor class separation, $1 \leq$ SDI < 3 indicates good separation, and SDI $\geq$ 3 indicates very good separation. This method has been successfully applied to the assessment of spectral indices by researchers such as Piyoosh and Ghosh [24], Bouhennache et al. [25] and Su et al. [53].

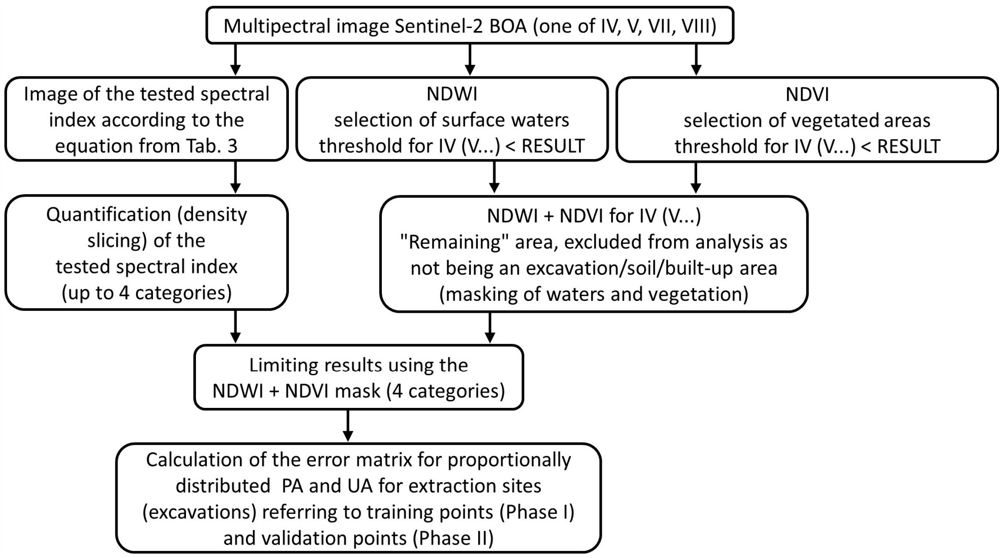

Figure 4. Workflow illustrating the verification stages of the indices' performance.

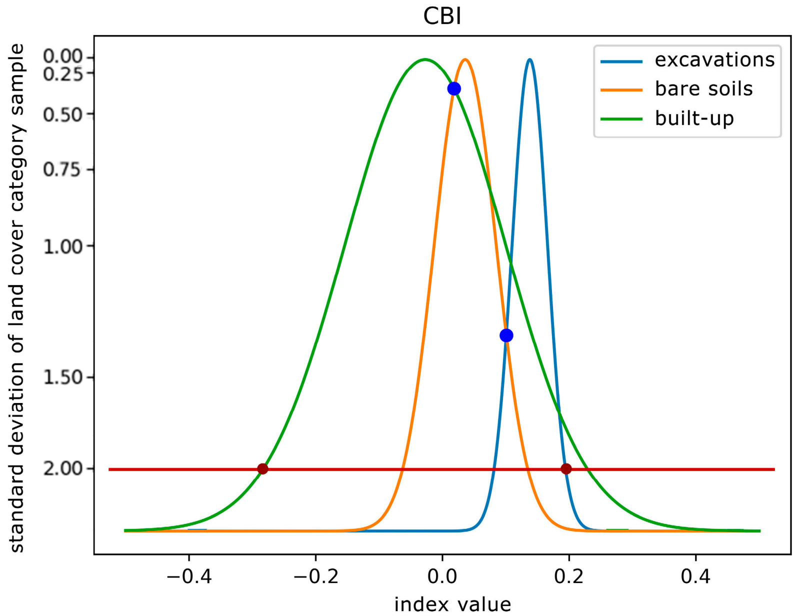

Figure 5. Determination of threshold values between classes (blue points) by overlaying the distributions of the three sampled classes. Exclusion of the range above twice the standard deviation (red points). Example for the CBI index. X-axis—index value; Y-axis—distance from class sample means; both are expressed in terms of their standard deviations.

It is easy to see that only a few of the tested spectral indices exceed an SDI value of 1. These are generally low values, which result from the significant spectral similarity of the three classes compared at the beginning, as previously mentioned. The obtained SDI results became one of the premises for the selection and choice of key indices for further stages of work.

As thresholds for class recognition across the entire surface of the index images, equal distances between pairs of classes were adopted, arranged according to increasing average, and expressed in multiples of standard deviations of their samples (standardized distance). This approach allows a balance to be maintained between overestimation errors (1-UA) and underestimation errors (1-PA) of classes separated by the threshold (2).

$$\begin{aligned} \text{threshold}_{a-b} &= \mu_a + \delta_a \times \text{SDI}_{a-b} \quad \text{if } \mu_a < \mu_b \\ \text{threshold}_{a-b} &= \mu_a + \delta_b \times \text{SDI}_{a-b} \quad \text{if } \mu_a < \mu_b \end{aligned} \tag{2}$$

where a, b are classes separated by the threshold value SDI_{a-b}, according to (1).

The methodology for establishing classification thresholds is graphically elucidated in Figure 5, which illustrates the intersections of the exponential functions representing the normal distribution curves of the spectral values for each pair of land cover categories.

Extreme thresholds (minimum and maximum) were established at twice the standard deviation from the mean for the classes with the lowest and highest averages, respectively (indicated by red points in Figure 5). Through the process of quantization, commonly referred to as 'density slicing' in remote sensing, four distinct categories were delineated from each spectral index: excavation, bare soils, built-up areas, and 'other'—a category encompassing areas not classified within the three primary classes, with index values falling outside the extreme threshold limits. Table 4 presents the characteristics of the class samples and the threshold values set for the three indices that demonstrated the highest effectiveness in SDI for excavation detection.

Table 4. Compilation of the most efficient spectral indices for the detection of excavations, bare soils, and built-up areas (in alphabetical order). Test field III. The most significant values determining the choice of the index are highlighted.

Index	Excavation			
	PA	UA	$\frac{PA+UA}{2}$	$\frac{SDI_{exc-soi*}+SDI_{exc-bui*}}{2}$
CBI	92.65	76.46	84.56	1.190
NBAI_B	88.53	76.59	82.56	1.113
NBAI_G	90.29	78.52	84.41	1.195
NBI	77.65	75.21	76.43	1.116
RNDSI	81.76	78.98	80.37	0.921
ShDI	85.53	77.60	80.57	1.022
3BUI	75.00	72.65	73.83	1.060
Index	**Bare soils**			
	PA	UA	$\frac{PA+UA}{2}$	$SDI_{exc\text{-}soi}$
BLFEI	67.11	79.39	73.31	1.259
BRBA	67.35	84.81	76.08	1.535
BSI	80.00	71.39	75.70	0.760
BSI_1	83.53	73.58	78.56	0.998
DBSI	88.24	75.95	82.10	1.054
PISI	67.89	75.21	71.59	0.708
3BUI	75.59	81.07	78.33	0.743
Index	**Built-up**			
	PA	UA	$\frac{PA+UA}{2}$	$SDI_{(exc\text{-}soi)\text{-}bui}$
BAEI	72.94	78.98	75.96	0.982
NBI	73.53	73.96	73.75	0.964
IRI_SWIR1	68.22	65.88	67.10	0.754

* Meaning of subscripts: exc-soi (excavation—soil), exc-bui (excavation—built-up).

As previously mentioned, the tested indices were designed by their creators for the detection of soils and/or built-up areas. This task is understood and implemented in various ways—some indices facilitate the detection of these classes relative to others, while some primarily enable the differentiation between soils and built-up areas. The latter group of indices often incorrectly separates these classes from others, even those as spectrally distinct as surface waters and vegetation (e.g., with very low SDI values). Therefore, to assess the actual utility of both groups of indices for the detection of excavations, a mask was applied to the quantization result, which excluded forested areas, low vegetation, and waters from the analysis. For this purpose, indices such as the NDVI (Normalized Difference Vegetation Index) and the NDWI (Normalized Difference Water Index) were utilized. Only then did the corrected class maps constitute the final result.

$$NDVI = \frac{NIR - Red}{NIR + Red} = \frac{B08 - B04}{B08 + B04} \tag{3}$$

$$NDWI = \frac{Green - NIR}{Green + NIR} = \frac{B03 - B08}{B03 + B08} \tag{4}$$

The practical assessment of the utility of indices is most commonly based on the accuracies of the classes, kappa coefficients, and the overall accuracy of classification (see [10,13,25,26,28,31,40]). This approach was also adopted here for the analysis of the performance of the tested indices. The subsequent stages of the actions performed are presented in Figure 4.

In the first stage, as outlined in Figure 4, accuracy metrics were calculated in reference to the training points, which were treated as 'ground truth' for the computed error matrix. The average Spectral Discrimination Index (SDI) results for the extraction sites (5) were compared with the average producer's accuracy (PA) and user's accuracy (UA) (6), obtained for this class (Figure 6).

$$SDI_{\text{avg\_exc}} = \frac{SDI_{\text{exc-soi}} + SDI_{\text{exc-bui}}}{2} \tag{5}$$

$$PA_{\text{UA\_avg\_exc}} = \frac{PA_{\text{exc}} + UA_{\text{exc}}}{2} \tag{6}$$

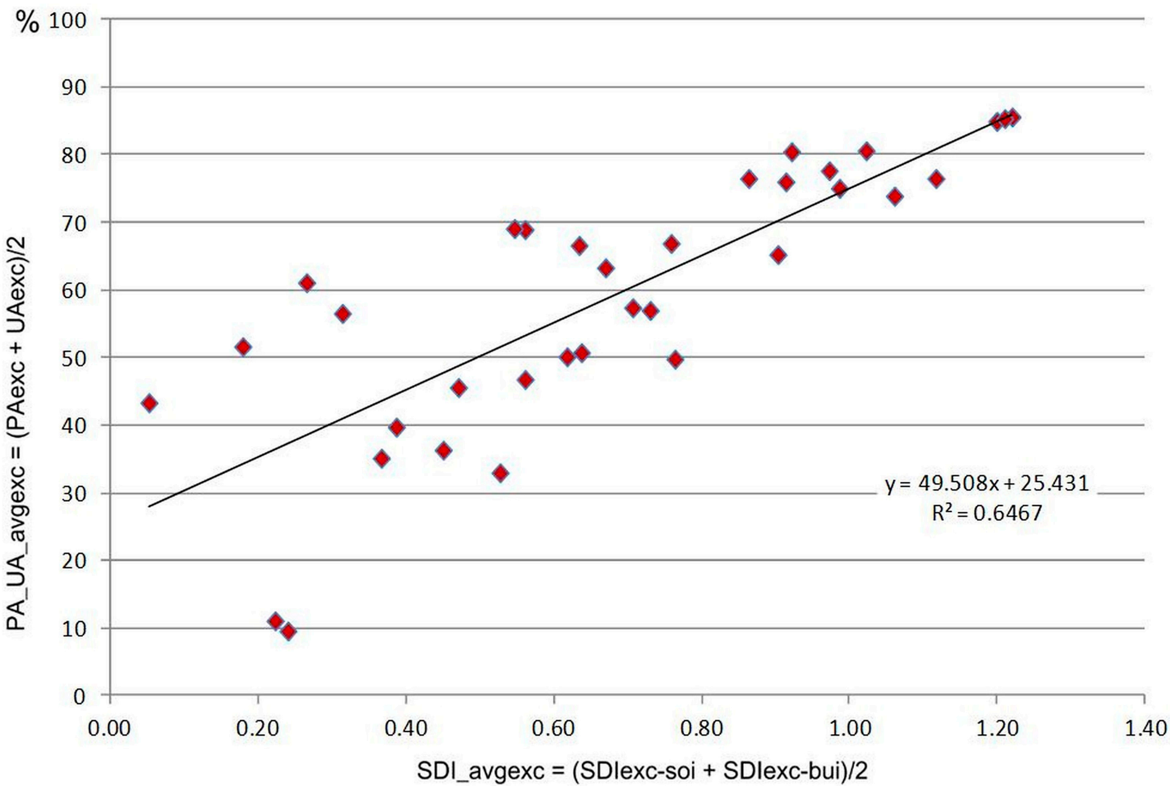

Figure 6. Relationship between the Spectral Discrimination Index (SDI) parameters (5) and the accuracy metrics obtained for the class of excavations (6), based on training points, test field C, across 34 indices.

As illustrated in Figure 6, the correlation between the Spectral Discrimination Index (SDI) for the entire set of 34 indices and the accuracy metrics is represented by a coefficient of determination (R^2) of 64.7%, with a correlation coefficient (r) of 0.804. This relationship strengthens for indices with higher SDI values. By excluding results for SDI_avg$_{\text{exc}}$ less than 0.35, the coefficient of determination (R^2) increases to 75.7%, with a correlation coefficient (r) of 0.870.

Three indices with the highest SDI values (CBI, NBAI_B, NBAI_G) also achieved the highest PA and UA values, averaging around 84%, which is approximately 4% higher than the subsequent indices (Table 4). Among this trio, the choice of CBI is supported by the highest SDI coefficient for the soil–urban area pair (0.36), compared to lower values for NBAI_B (0.24) and NBAI_G (0.18). The CBI also records the highest potential for excavation detection (PA = 92.65%), albeit at the expense of a slightly lower reliability (UA = 76.46%). In subsequent steps, solutions aimed at improving the UA values for the CBI index were sought.

The high efficiency of the first three indices can be explained by analyzing the spectral response of the main types of land cover present in the study area. Figure 7 shows the spectral curves, developed based on the average spectral responses from the training points. Mining areas are characterized by the highest reflectance (except in the NIR, where vegetation dominates), followed by exposed soils and built-up areas. The patterns of the curves for these three types of land cover are quite similar in shape.

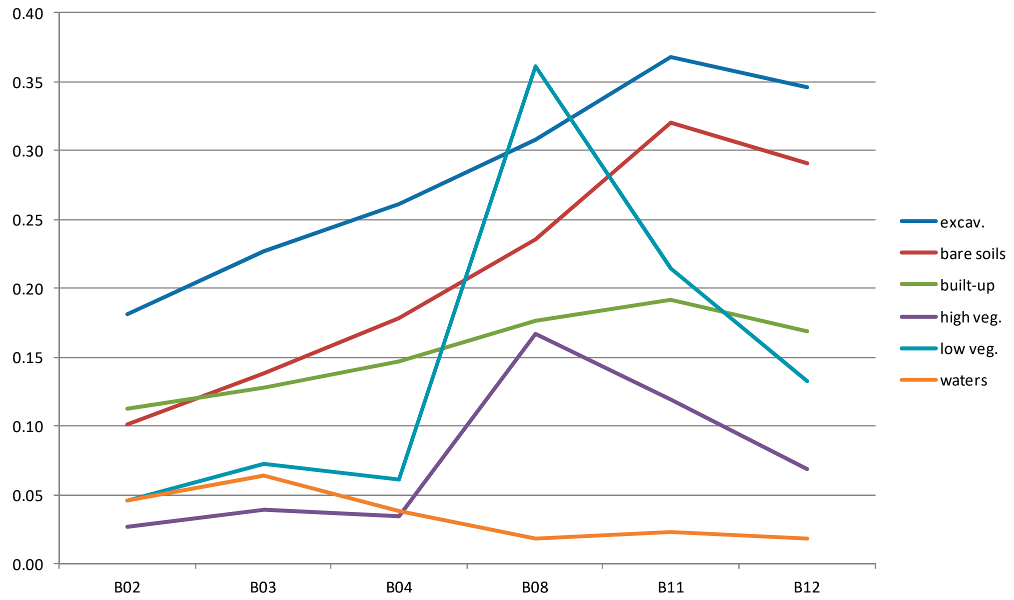

Figure 7. Spectral curves of the 6 main land cover categories, based on training points. Y-axis—spectral reflectance value (albedo).

It seems that distinguishing mining areas from other land cover categories should be relatively easy. However, an analysis of the variability of individual class samples indicates their high degree of overlap (Figure 8). Therefore, the simple use of channels alone is not sufficient to correctly separate these classes. Based on the following comparisons, it can be observed that in visible channels there is a greater (though still small) differentiation between mining areas and exposed soils than in infrared channels, especially SWIR. In these channels, there is a significant mixing of spectral responses between mining areas and built-up areas. The situation reverses in the infrared channels, particularly in SWIR. In these channels, the mixing of built-up areas with mining sites is reduced, but unfortunately, there is an increased spectral similarity between mining areas and soils. There is also spectral overlap between vegetation and mining areas, especially in the NIR channel and, to a lesser extent, SWIR1. The natural consequence of these observations is the complementary use of visible channels along with mid-infrared channels, with a particular emphasis on SWIR2. This task is accomplished by indices such as CBI, NBAI_B, and NBAI_G, although the mechanism of CBI differs from that of the NBAI indices.

The NBAI_B index compares SWIR2 values with the proportion of the NIR channel relative to the blue channel, while the NBAI_G index compares SWIR2 values with the proportion of SWIR1 to Green. Since the curves for exposed soils and built-up areas lie below the curve for mining areas, these ratios will have a higher value for these classes than for mining areas. This ratio will be higher even in situations where there is a steeper slope of the curve for mining areas, as is the case compared to the curve for built-up areas. Therefore, the design of indices in this group allows for an additional emphasis on the difference in reflectance increase between mid-infrared SWIR radiation and the visible area for the mining class.

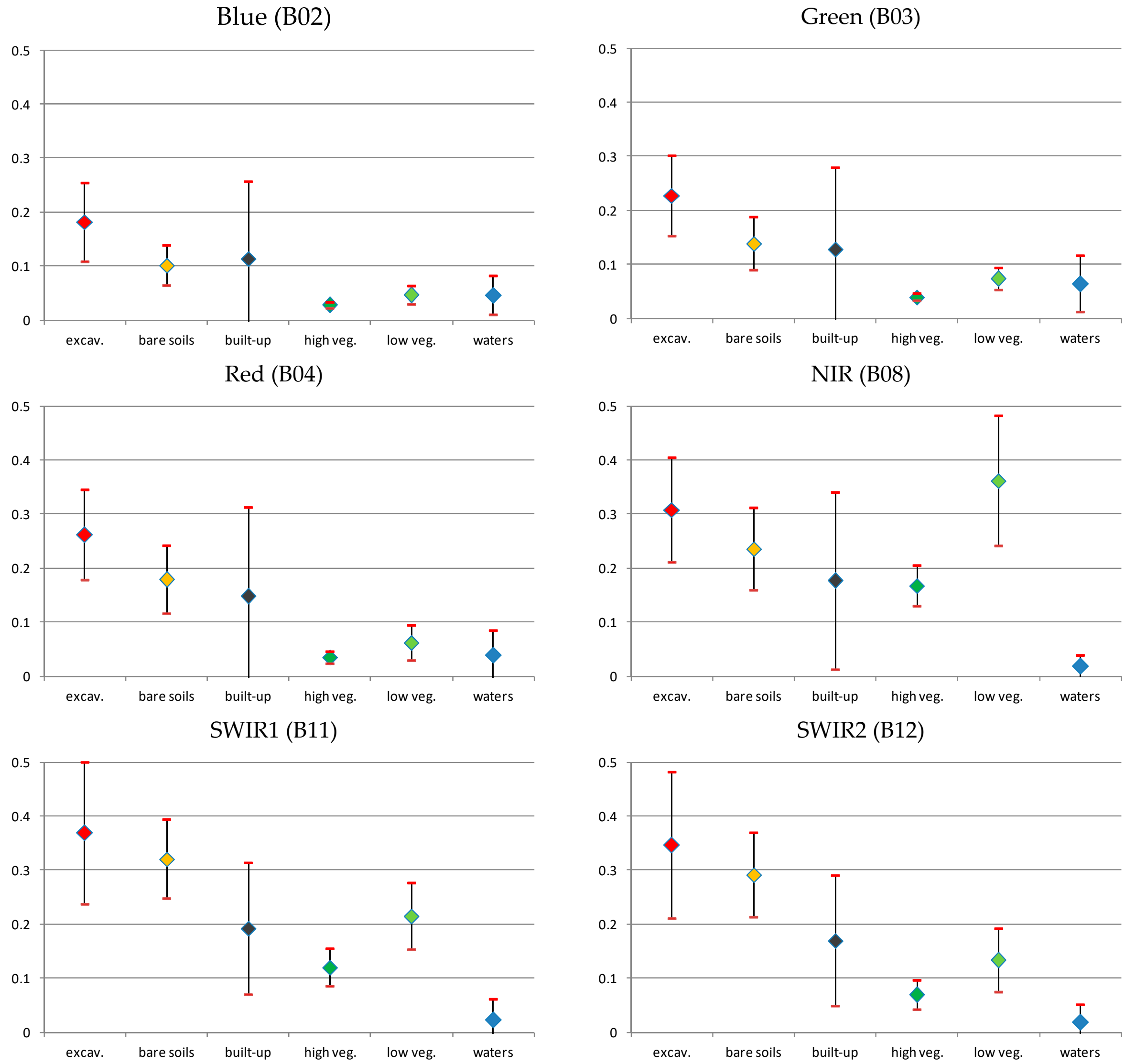

Figure 8. Average spectral responses of the six main land cover categories for six Sentinel-2 bands. Vertical lines indicate the range of $\pm 2 \times$ SD (Standard Deviation).

The CBI index is a complex indicator, based on principal component transformation and two indices, NDWI and SAVI. The first principal component, PC1, dynamically constructs, based on the correlation matrix, a new range of image brightness, primarily averaging information from highly correlated visible channels. Combined with the surface water detection index, it provides a stable average, resistant to changes in land cover that may occur in different research areas. This average is built on opposite objects in terms of brightness: exposed soil and excavations (in PC1) and surface water (in NDWI). Comparing such an image to the value of a biomass index that considers the influence of soil background effectively differentiates areas with the highest reflectance from others, as in practice, only these record positive index values. Simultaneously, there is a reduction in the differentiation between water and vegetation areas. Only for the darkest surface waters, similarly to objects with high reflectivity, can a positive index value occur, which can confuse the result for these classes. This explains why the CBI index requires the application of an additional mask to eliminate water classes, which can be traced by comparing Figure 9A with B and Table 5A with B.

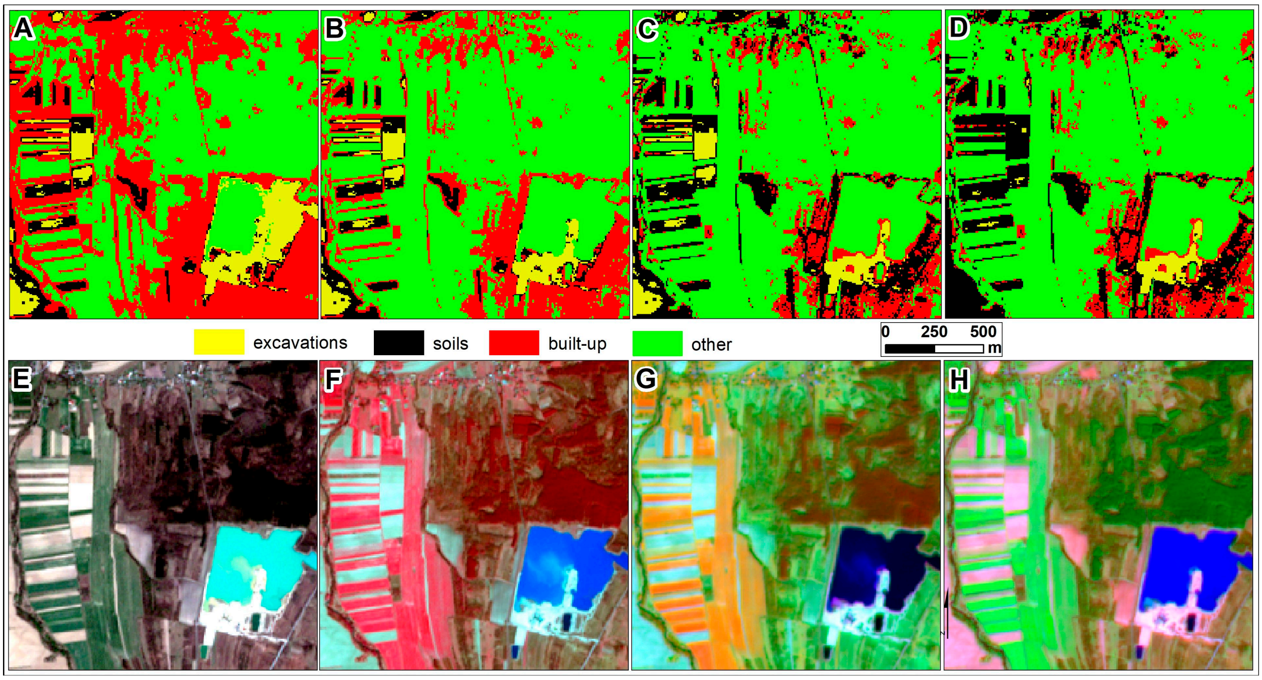

Figure 9. Fragment of Test Field III—gravel pit area; classification result according to the decision algorithm: the letter designations (**A**–**D**) correspond to the error matrices (**A**–**D**) from Table 6; (**E**–**H**): background image © EU-Sentinel. Sentinel-2. 5 April 2019. L2A_T34UDA_A019767_20190405T094119: (**E**) CC TC, (**F**) FCC CIR, (**G**) FCC 1, (**H**) FCC 2.

Table 5. Summary of class accuracies demonstrating the effectiveness of each segment of the decision-making scheme presented in Figure 10. Applied to test field III, variant A.

BLOCK II (CBI Only, without BAEI, BRBA)							
A		Ground Truth File					
		excav.	Bare Soils	Built-Up	Rest	Total	UA [%]
classification result according to the decision algorithm	excavations	325	74	60	55	514	63.23
	bare soils	15	177	70	92	354	50.00
	built-up	0	89	201	237	527	38.14
	other	0	0	9	636	645	98.60
	total	340	340	340	1020	2040	
	PA [%]	95.59	52.06	59.12	62.35		OA = 65.64
BLOCK II (CBI only, without BAEI, BRBA), BLOCK III							
B		ground truth file					
		excav.	Bare soils	built-up	rest	total	UA [%]
classification result according to the decision algorithm	excavations	325	74	60	0	459	70.81
	bare soils	15	177	70	0	262	67.56
	built-up	0	89	201	5	295	68.14
	other	0	0	9	1015	1024	99.12
	total	340	340	340	1020	2040	
	PA [%]	95.59	52.06	59.12	99.51		OA = 84.22

Table 5. *Cont.*

BLOCK II (CBI, BAEI, BRBA), BLOCK III							
C		ground truth file					
		excav.	Bare soils	built-up	rest	total	UA [%]
classification result according to the decision algorithm	excavations	308	74	26	0	408	75.49
	bare soils	9	187	24	1	221	84.62
	built-up	23	79	285	4	391	72.89
	other	0	0	5	1015	1020	99.51
	total	340	340	340	1020	2040	
	PA [%]	90.59	55.00	83.82	99.51		OA = 87.99
BLOCK II (CBI, BAEI, BRBA), BLOCK III, BLOCK I							
D		ground truth file					
		excav.	bare soils	built-up	rest	total	UA [%]
classification result according to the decision algorithm	excavations	307	5	26	0	338	90.83
	bare soils	10	256	24	1	291	87.97
	built-up	23	79	285	4	391	72.89
	other	0	0	5	1015	1020	99.51
	total	340	340	340	1020	2040	
	PA [%]	90.29	75.29	83.82	99.51		OA = 91.32

The average overestimation error for excavations using the CBI index for test field III is 23.5%. A detailed error matrix analysis reveals that uncovered soils account for 13.5% of the overestimation, while built-up areas represent 10.0%. No overestimation errors were recorded for other areas (water, vegetation), confirming the effectiveness of the NDWI and NDVI indices in masking classes secondary to excavations. To improve the user's accuracy (UA), it is necessary to eliminate as many false detections of excavations as possible while maintaining a high producer's accuracy (PA). Therefore, additional indices with very high reliability in identifying soils and built-up areas were sought to be used complementarily with the CBI index.

As previously performed for the excavation class (see Figure 4), accuracies for the uncovered soil and built-up classes were calculated for individual indices. Table 5 lists the results with the highest UA values, maintaining a PA greater than 65%. The most reliable identification of uncovered soils was achieved with the BRBA index (UA = 84.81%), and for built-up areas with the BAEI index (UA = 78.98%). The high UA values and relatively high SDI in relation to the excavation class indicate that additional indices will 'correct' some areas misclassified by the CBI as excavations to the correct classes, i.e., uncovered soils or built-up areas.

Furthermore, changes within a single vegetation season were utilized. Having multi-temporal images allowed for the verification of whether vegetation, even if only periodically, appeared in areas identified as excavations. If so, this would indicate a misclassification of the area as an excavation and necessitate correction to uncovered soils.

By integrating these individual actions, a final decision-making scheme was developed (Figure 10), based on a total of 5 spectral indices. 'Block I' includes multitemporal analysis using NDVI. 'Block II' presents the results of the CBI index with improved UA for excavations, achieved through the BAEI and BRBA indices. 'Block III' is a mask that eliminates areas of water and vegetation for the given data acquisition period. Threshold values were calculated separately for each of the three study areas. Variant A applies average multi-month threshold values, while variant B uses monthly optimized averages for each registration period (different vegetation periods).

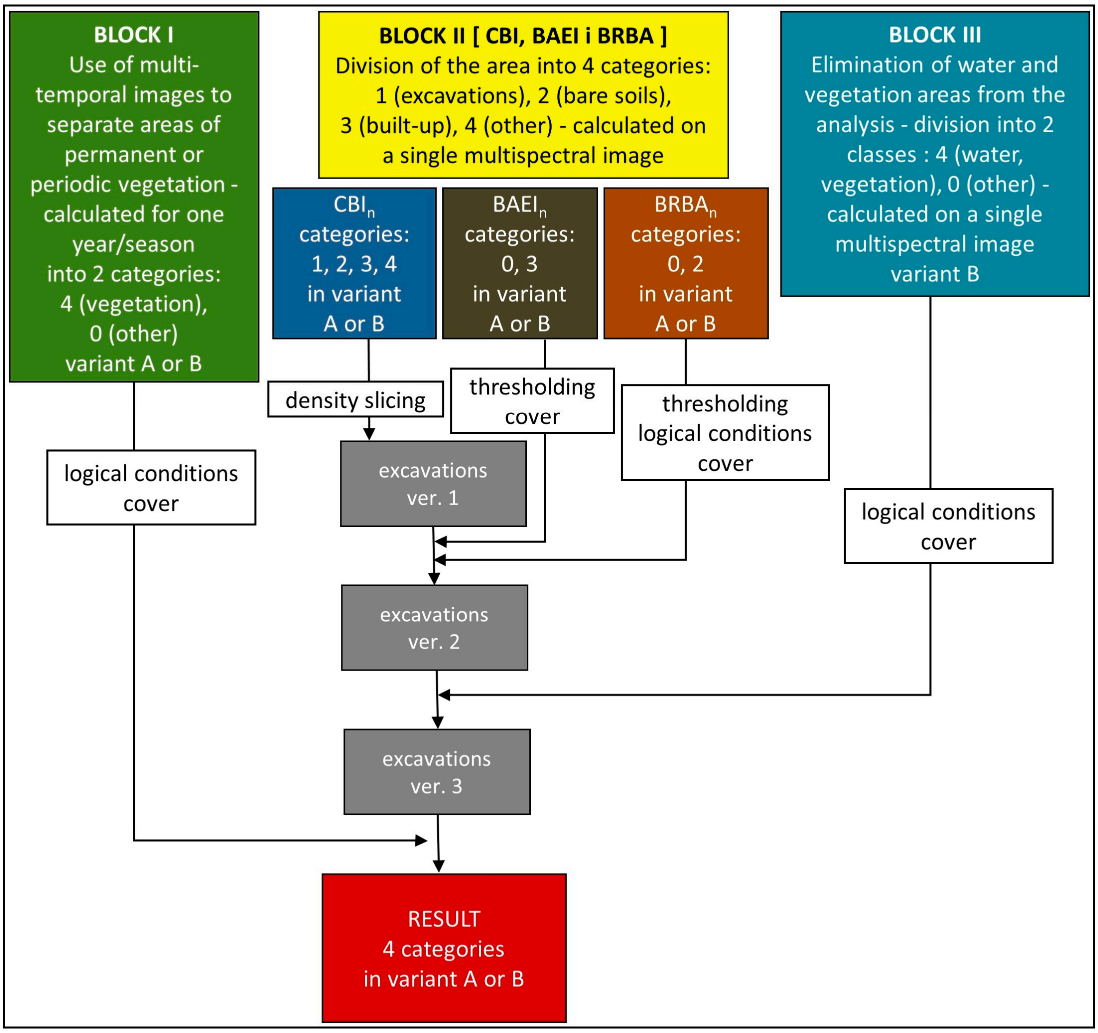

Figure 10. Flowchart for the detection of excavations, illustrating two thresholding approaches: variant A applies average thresholds derived from multiple months for a given area (I, II, III); variant B employs thresholds dedicated to a specific area and month of data acquisition.

Table 5 and Figure 9 demonstrates the impact of each analytical block element on the final excavation detection results. It presents the accuracies for four classes (1—excavations; 2—exposed soils; 3—built-up areas; 4—other) derived from the April 2019 data for the training area (test field III). The figure also includes a segment of the resulting image from test field III (Figure 10), depicting an excavation site (gravel pit) adjacent to agricultural and forested lands.

Table 5 and Figure 9 trace the influence of each block element on the excavation recognition process. Initially, using only the CBI index (part A, Table 6, Figure 9) leads to high producer's accuracy but low user's accuracy due to overclassification of the excavation class. Introducing a water and vegetation mask (part B) corrects misclassifications over water bodies, enhancing user's accuracy (see Figure 9). Further refinement using BRBA and BAEI indices (part C) improves the overall accuracy for all four classes. The multitemporal analysis block (part D) fine-tunes the excavation class recognition, balancing both user's and producer's accuracies.

4. Results and Discussion

The results of identifying areas of surface resource extraction are presented in Figure 11. The detected areas for the scene from August, in Area II, are showcased.

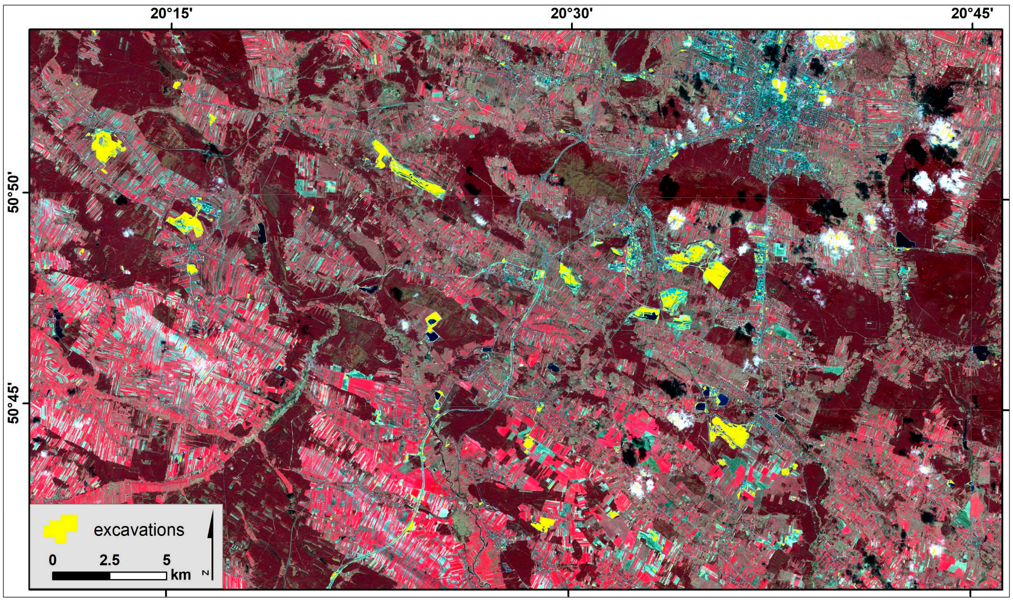

Figure 11. Test site II (August 2019) with distinguished excavations (in yellow) requiring field control. Background image © EU-Sentinel. Sentinel-2. 15 April 2019, L2A_T34UDB_A019910_20190415T094033.

As can be observed, the developed methodology enables the automatic recognition of various areas, including quarries, mines, and storage sites of extracted building materials (refer to Figure 12). The cyclic utilization of up-to-date scenes, recorded by the Sentinel-2 satellite, allows for the ongoing monitoring of the size and changes in the designated extraction areas, as well as the detection of emerging new areas. Comparing these data with databases of registered mining concession sites enables the identification of areas requiring field inspection. Key in this context is understanding the reliability of such indications and being aware of the potential for overlooking certain situations.

The developed methodology and the expected benefits of applying an expanded scheme of indicators required validation on independent sets of control points, appropriately stratified. The main problem in their preparation was the significant surface area disparity of the "excavation" class compared to other classes. Excavations account for about 0.43% of the total mineral area in test field I and up to 23.10% in test field II (see Table 6 and Figure 13). Random allocation of points across the entire area (weighted method) would result in a small number of control points in the key excavation recognition area. On the other hand, adopting an equal number of points for each class (as was used in the learning phase) would inflate the consumer's accuracy for the "excavation" class. An intermediate solution was adopted here, following Olofsson et al. [54], where the number of points allocated to the "excavation" and "non-excavation" classes are averages of both approaches, with the overriding assumption that there should be about 50 control points per 1 km^2 of land. Details of the calculations are included in Table 6. Differences between the theoretically calculated number of points and the number actually used result from inaccuracies in the algorithms randomly generating points for the indicated polygons.

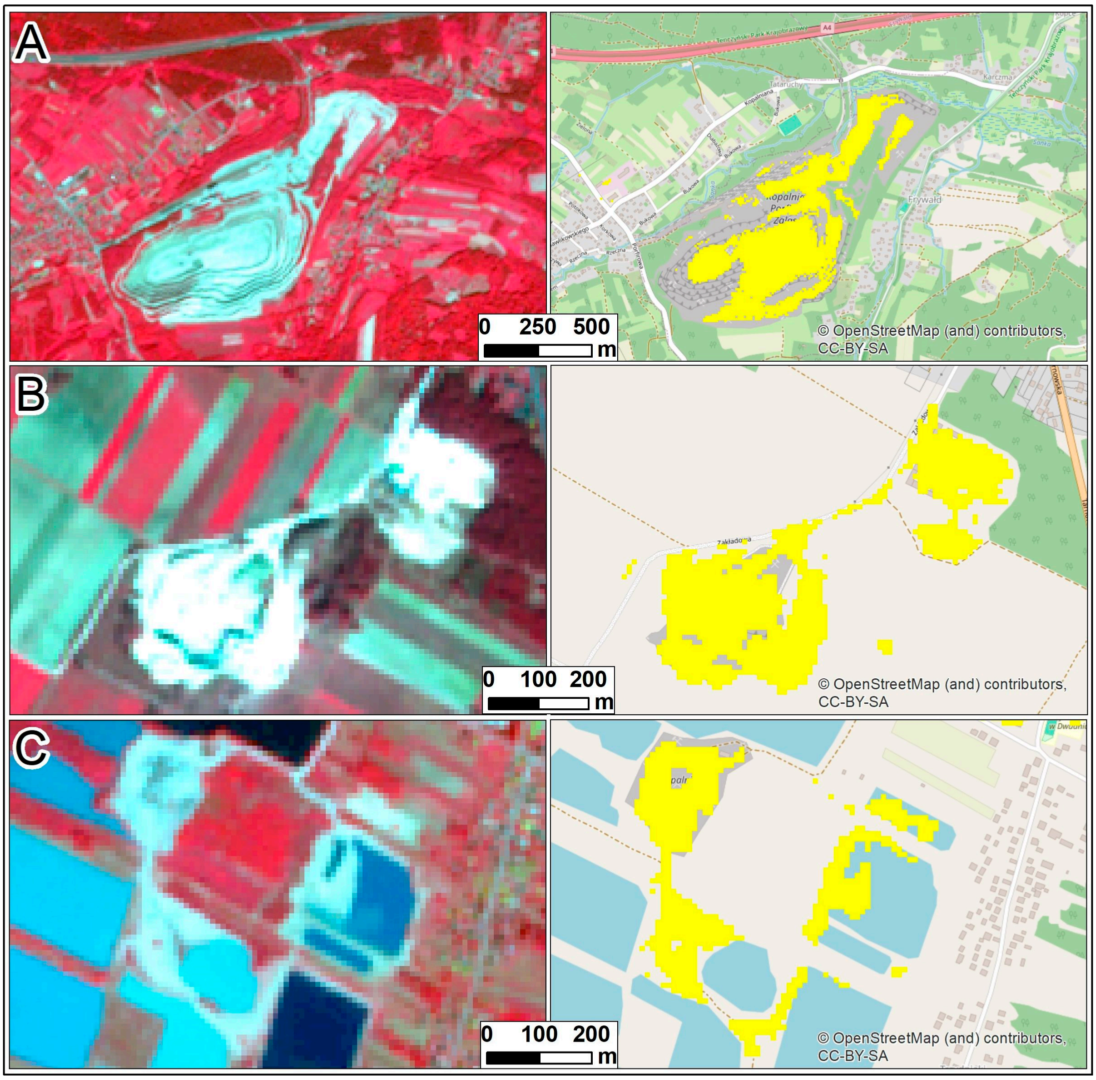

Figure 12. Fragments of test areas with identified diverse open-pit mining objects (on the left): Background image © EU-Sentinel. Sentinel-2. FCC CIR: (**A**) Area I—19 June 2019 (L2A_T34UCA_A011788_20190609T094208), porphyry mine (quarries); (**B**) Area II—15 April 2019 (L2A_T34UDB_A019910_20190415T094033), 'Wola Morawicka' Limestone Quarry (open-pit with mineral stockpile); (**C**) Area III—29 July 2019 (L2A_T34UDA_A012503_20190729T094242), aggregate mine (gravel pit) ZEK in Dwudniaki. The recognition results are marked in yellow on the OpenStreetMap background.

The accuracy assessments conducted on control points across the three test sites (I, II, III) for the various acquisition dates (April to September) and their corresponding averaged values are presented in Table 7. The table delineates the accuracy metrics achieved for the excavation class employing: (1) solely the CBI index complemented by a mask for water and vegetation (as delineated in 'Block III'); (2) a combination of CBI, BRBA, and BAEI indices alongside the water and vegetation mask (as outlined in 'Block III'); and (3) a comprehensive framework incorporating the multitemporal analysis block (integrating CBI, BRBA, BAEI, 'Block I', and 'Block III'). Each methodological approach, namely (1), (2), and (3), was executed under two scenarios: Variant A, which utilizes mean threshold values derived from the months of April to September, and Variant B, which applies thresholds specifically tailored for each month. For the synthetic datasets (mean and standard deviations) listed in the lower section of the table, the most favorable (indicated in green) and least favorable (indicated in red) outcomes for the evaluated scenarios are indicated.

Initial assessments, conducted on a training subset and based on the analysis of SDI values along with accuracy metrics, underscored the necessity for devising a comprehensive suite of indicators. This stemmed from the observation that no single indicator fulfilled the anticipated objective of high-reliability excavation detection. Each of the five indicators, ultimately incorporated into the decision-making framework, was intended to fulfill a specific function: water detection (NDWI), vegetation (NDVI), excavation sites (CBI), exposed soil (BRBA), and built-up areas (BAEI). The results documented (refer to error matrices in Table 5, Figure 10) suggested the feasibility of enhancing the overall accuracy of excavation identification.

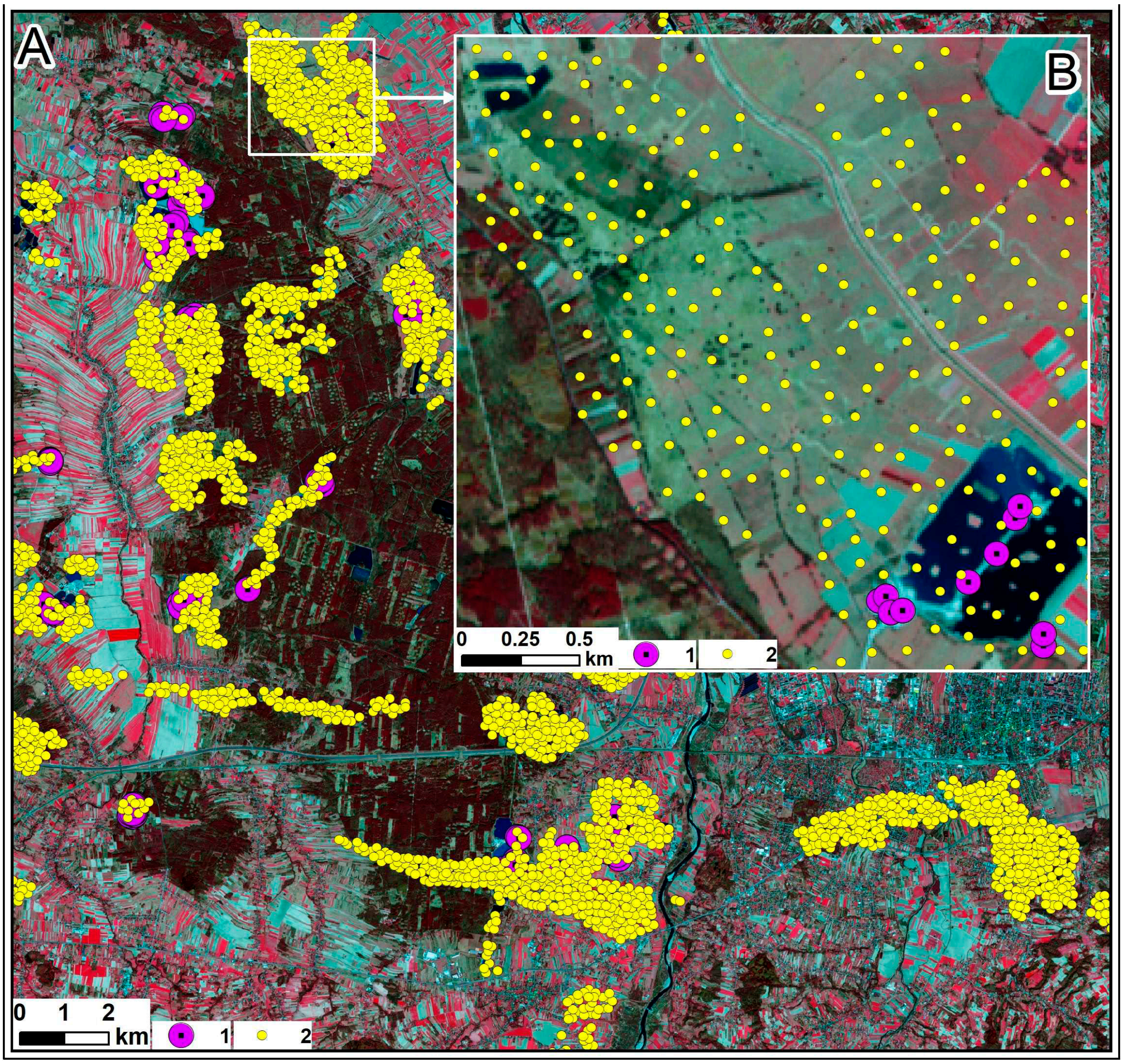

Figure 13. Example distribution of control points against a background of minerals (test field III); 1—excavations; 2—other land cover classes within the mineral areas. Background image © EU-Sentinel. Sentinel-2. 5 April 2019, FCC CIR (L2A_T34UDA_A019767_20190405T094119).

Table 6. Summary of calculations associated with the preparation of stratified control samples for three areas of analysis.

Test Areas	Parameter	Excavations in Mineral Areas	Minerals/Minerals without Excavations
Test field I 2430.64 km^2	km^2	4.87	1128.21/1123.34
	Weighted Sample (at 100 pts/km)	487	112,334
‘Exc’/‘Min’ Ratio 1/230.67	Equal Sample (at 100 pts/km for “Exc”)	487	487
Exc = 0.43%	Average from equal and weighted method	(487 + 487)/2 = 487	(487 + 112,334)/2 = 56,411
of mineral area	Final adopted sample	491	54,776
Test field II 1057.36 km^2	km^2	6.44	34.32/27.86
	Weighted Sample (at 100 pts/km)	644	2786
‘Exc’/‘Min’ Ratio 1/4.33	Equal Sample (at 100 pts/km for “Exc”)	644	644
Exc = 23.10%	Average from equal and weighted method	(644 + 644)/2 = 644	(644 + 2786)/2 = 1715
of mineral area	Final adopted sample	644	1689
Test field III 700.53 km^2	km^2	1.86	66.74/64.88
	Weighted Sample (at 100 pts/km)	186	6488
‘Exc’/‘Min’ Ratio 1/34.88	Equal Sample (at 100 pts/km for “Exc”)	186	186
Exc = 2.87%	Average from equal and weighted method	(186 + 186)/2 = 186	(186 + 6488)/2 = 3337
of mineral area	Final adopted sample	186	3242

Table 7. Detection accuracies for excavation areas utilizing the decision-making scheme depicted in Figure 9 across Test Fields I, II, and III. The results are based on a stratified control sample, with color coding to indicate performance: red denotes the least favorable outcome that discriminates against the variant in question, while green signifies the most favorable or optimal result.

Test Field	Months	Index	CBI + BLOCK III		CBI, BAEI, BRBA + BLOCK III		CBI, BAEI, BRBA+ BLOCK III + BLOCK I (Multitemporal)	
			Variant A	Variant B	Variant A	Variant B	Variant A	Variant B
I	IV	PA	84.3	76.2	55.2	51.5	55.2	51.5
		UA	27.1	33.0	26.4	29.8	36.5	38.5
		$\frac{PA+UA}{2}$	55.7	54.6	40.8	40.7	45.8	45.0
	VI	PA	92.3	76.0	74.1	69.9	74.1	69.9
		UA	20.4	35.1	34.9	42.3	36.8	43.5
		$\frac{PA+UA}{2}$	56.3	55.5	54.5	56.1	55.5	56.7
	VII	no image data						
	VIII	PA	11.4	75.6	10.6	60.3	10.6	60.3
		UA	44.4	34.0	45.6	47.5	46.4	48.8
		$\frac{PA+UA}{2}$	27.9	54.8	28.1	53.9	28.5	54.5
	IX	PA	65.6	73.1	49.3	61.1	49.3	61.1
		UA	41.9	39.0	46.4	44.2	47.2	45.4
		$\frac{PA+UA}{2}$	53.7	56.1	47.8	52.6	48.2	53.2
	mean	PA	63.4	75.2	47.3	60.7	47.3	60.7
		UA	33.5	35.3	38.3	41.0	41.7	44.1
		$\frac{PA+UA}{2}$	48.4	55.3	42.8	50.8	44.5	52.4

Table 7. *Cont.*

Test Field	Months	Index	CBI + BLOCK III		CBI, BAEI, BRBA + BLOCK III		CBI, BAEI, BRBA+ BLOCK III + BLOCK I (Multitemporal)	
			Variant A	Variant B	Variant A	Variant B	Variant A	Variant B
II	IV	PA	79.0	81.1	74.7	75.9	74.7	75.9
		UA	89.8	88.8	89.9	89.1	90.8	89.9
		$\frac{PA+UA}{2}$	84.4	84.9	82.3	82.5	82.7	82.9
	VI	PA	93.9	93.2	89.3	89.6	89.3	89.6
		UA	87.2	88.6	89.3	89.6	89.3	89.7
		$\frac{PA+UA}{2}$	90.6	90.9	89.3	89.6	89.3	89.7
	VII	PA	84.5	89.9	82.9	82.1	82.9	82.0
		UA	90.5	89.5	90.5	89.8	90.7	90.3
		$\frac{PA+UA}{2}$	87.5	89.7	86.7	86.0	86.8	86.1
	VIII	PA	90.1	88.0	86.8	82.9	86.7	82.6
		UA	87.9	89.3	88.5	89.9	89.6	91.3
		$\frac{PA+UA}{2}$	89.0	88.7	87.6	86.4	88.1	86.9
	IX	PA	87.0	85.4	79.5	82.1	79.2	81.7
		UA	91.1	91.7	92.3	92.5	93.9	94.3
		$\frac{PA+UA}{2}$	89.0	88.5	85.9	87.3	86.6	88.0
	mean	PA	86.9	87.5	82.6	82.5	82.5	82.4
		UA	89.3	89.6	90.1	90.2	90.9	91.1
		$\frac{PA+UA}{2}$	88.1	88.5	86,4	86.4	86.7	86.7
III	IV	PA	74.2	69.9	71.5	65.1	71.5	65.0
		UA	68.0	76.0	71.1	79.1	78.7	82.3
		$\frac{PA+UA}{2}$	71.1	73.0	71.3	72.1	75.1	73.7
	VI	no image data						
	VII	PA	88.7	90.9	83.9	85.5	83.9	85.0
		UA	77.8	70.4	82.1	72.3	85.3	83.6
		$\frac{PA+UA}{2}$	83.3	80.6	83.0	78.9	84.6	84.3
	VIII	PA	85.0	86.0	80.1	76.3	79.6	74.7
		UA	81.4	80.0	81.4	80.2	84.1	86.3
			83.2	83.0	80.8	78.3	81.8	80.5
	IX	PA	79.0	79.0	65.6	74.2	64.5	72.6
		UA	81.7	79.0	84.1	81.2	89.6	86.5
		$\frac{PA+UA}{2}$	80.4	79.0	74.9	77.7	77.0	79.6
	mean	PA	81.7	81.5	75.3	75.3	74.9	74.3
		UA	77.2	76.4	79.7	78.2	84.4	84.7
		$\frac{PA+UA}{2}$	79.5	78.9	77.5	76.7	79.7	79.5

Table 7. *Cont.*

Test Field	Months	Index	CBI + BLOCK III		CBI, BAEI, BRBA + BLOCK III		CBI, BAEI, BRBA+ BLOCK III + BLOCK I (Multitemporal)	
			Variant A	Variant B	Variant A	Variant B	Variant A	Variant B
total, meansofI + II + III	IV	PA	79.2	75.7	67.1	64.2	67.1	64.1
		UA	61.6	65.9	62.5	66.0	68.7	70.2
		$\frac{PA+UA}{2}$	70.4	70.8	64.8	65.1	67.9	67.2
	VI	PA	93.1	84.6	81.7	79.8	81.7	79.8
		UA	53.8	61.9	62.1	66.0	63.1	66.6
		$\frac{PA+UA}{2}$	73.5	73.2	71.9	72.9	72.4	73.2
	VII	PA	86.6	90.4	83.4	83.8	83.4	83.5
		UA	84.2	80.0	86.3	81.1	88.0	87.0
		$\frac{PA+UA}{2}$	85.4	85.2	84.9	82.5	85.7	85.2
	VIII	PA	62.2	83.2	59.2	73.2	59.0	72.5
		UA	71.2	67.8	71.8	72.5	73.4	75.5
		$\frac{PA+UA}{2}$	66.7	75.5	65.5	72.9	66.1	74.0
	IX	PA	77.2	79.2	64.8	72.5	64.3	71.8
		UA	71.6	69.9	74.3	72.6	76.9	75.4
		$\frac{PA+UA}{2}$	74.4	74.5	69.5	72.5	70.6	73.6
	mean	PA	77.3	81.4	68.4	72.8	68.2	72.5
		UA	66.7	67.1	69.4	69.8	72.3	73.3
		$\frac{PA+UA}{2}$	72.0	74.2	68.9	71.3	70.3	72.9
total, statistics ofI + II + III	SD	PA	21.5	7.5	21.3	11.4	21.3	11.2
		UA	25.7	24.1	23.8	22.2	22.7	21.6
			19.2	14.8	20.4	16.1	20.0	15.7
		PA-UA	27.8	20.1	19.1	14.3	18.3	14.0
		$\lvert PA - UA \rvert$	22.5	17.2	13.9	7.4	12.8	6.7
	min	PA	11.4	69.9	10.6	51.5	10.6	51.5
		UA	20.4	33.0	26.4	29.8	36.5	38.5
		$\frac{PA+UA}{2}$	27.9	54.6	28.1	40.7	28.5	45.0
	range	$\lvert PA - UA \rvert$	71.9	43.2	39.2	27.6	37.3	26.4
		PA	82.5	23.3	78.7	38.1	78.7	38.1
		UA	70.7	58.7	65.9	62.7	57.4	55.8

However, detailed analyses on control points revealed that the initial detection accuracies for CBI, when combined with the NDVI/NDWI mask (computed as the mean of PA and UA), did not exhibit improvement. The principal advantage of integrating additional indicators (BRBA and BAEI) and multitemporal analysis into the CBI was the average elevation of consumer accuracy by 6.6%. Concurrently, there was a moderate decline in producer accuracy, leading to a balanced PA and UA (with average-based discrepancies of less than 1%, in contrast to 9–14%, when solely employing the CBI index). Attaining a high overall class accuracy (OA), while equalizing producer (PA) and consumer (UA) accuracies across classes, is acknowledged as beneficial. This is among the criteria for evaluating various land cover and land use mapping methodologies (see [54–57]). Enhancements in outcomes from the CBI to the comprehensive scheme are observable in the table's last column, where numerous synthetic parameters attained optimal values (green), whereas the initial variants predicated solely on CBI recorded the least favorable consumer accuracy UA (66.7% and 67.1%).

Employing month-specific threshold values ('B' variants) yields, on average, results approximately 2.5% superior to those using mean threshold values from multiple months ('A' variants), with the exception of outcomes derived solely from the CBI index. The primary gain from applying distinct thresholds for each month is the stabilization of accuracy metrics. Utilizing mean thresholds led to pronounced fluctuations in PA/UA, which were offset by unexpectedly high values in alternate months. This is particularly evident in the test field I outcomes, where PA fluctuated from 10% (August) to 90% (June). With variable thresholds tailored for each month, these disparities ranged between 50% and 70%. A similar, albeit less pronounced, reduction in UA variability is noted in 'B' variants (ranging from 20–45% for mean thresholds to 33–47% for variable thresholds). These advantages of 'B' variants are discernible in the table's lower section, where unfavorable outcomes marked in red predominate in the 'B' variant columns, effectively disqualifying them as beneficial.

Across individual months, the results for May, August, and September are comparable, within an OA range of 70–75%. The lowest accuracies were observed in April. The highest average PA/UA values for July, as seen in Table 7, should be attributed to the absence of data from this period for test field I, which generally recorded lower accuracies for all months compared to the other two test areas.

The diminished accuracies for test field I result from a significant disparity between the mineral surface area and the excavation surface area (a mineral area 230 times larger than that of excavations). This discrepancy poses challenges in balancing the control sample, consequently diminishing accuracies, particularly UA (averaging 44% for test field I, versus 85% for test field II and 91% for test field III).

The potential for integrating machine learning (ML) and deep learning (DL) methods with spectral indicators in remote sensing for environmental monitoring, particularly in the detection of mining activities, is a growing area of research. Advanced ML algorithms such as random forest and support vector machines, as indicated in Carranza-García et al. (2019), have been successfully applied to classify land cover changes with improved accuracy [58,59]. These approaches can outperform traditional thresholding methods by effectively managing multidimensional datasets and extracting complex patterns.

Deep learning techniques, particularly convolutional neural networks (CNNs), have shown promising results in remote sensing feature extraction and classification tasks. A study by Carranza-García et al. [60], Robinson et al. [61], and Tahir et al. [62] demonstrated the effectiveness of DL in analyzing multispectral satellite imagery for environmental changes. DL models, combined with spectral indices, can greatly improve the detection of subtle landscape changes indicative of illegal mining activities.

Future research will focus on further leveraging ML and DL methodologies, adapting them to the unique challenges of remote sensing in environmental applications. This includes exploring new algorithmic approaches and integrating these techniques to more accurately detect and monitor illegal mining activities.

5. Summary and Conclusions

In summary, the integration of remote sensing technology in mining surveillance represents a step towards the adoption of low-carbon and non-polluting practices. By reducing the need for on-site inspections and enabling rapid assessments, the ecological footprint of monitoring operations can be significantly diminished. This aligns with the broader objectives of the circular economy, where resource efficiency and waste reduction are key.

Despite not achieving higher overall accuracies (averages of PA and UA values) in the recognition of excavations, the multi-indicator method (CBI + BRBA + BAEI + multitemporal) is a better solution compared to the CBI method alone. When comparing synthetic measures included in Table 7, it emerges as the method with the highest number of occurrences of beneficial values relative to other variants. It is also one of only two methods where critically poor values, marked in red in Table 7, do not occur (the other being the multi-indicator method without multitemporal analysis). It stabilizes the results obtained both across different months and test areas. Moreover, it reduces the differences between PA and UA accuracies. This means that monitoring, continuously conducted according to the proposed methodology, can provide predictable and reliable results even on a single set of Sentinel-2 data.

It is noteworthy that the accuracy calculations conducted on control points encompassed a substantial sample size. In some cases, such as test field I, despite using a mixed method for point stratification [54], several hundred points in the excavation area corresponded to tens of thousands of points in other classes (see Table 6). This automatically influenced the low UA values. However, it is clear that even with low UA values (33% to 44%), the area of potential illegal excavations will be greatly narrowed (e.g., for test field I from 1123 km^2 to about 15 km^2).

A drawback of the adopted solution is the necessity to establish threshold values for new areas when monitoring excavations each time (variant B). It is possible to forgo dedicated threshold values for each month (variant A), but this mainly results in a drop in producer accuracy of about 4%, while maintaining UA values. However, the negative effect of such simplification is a very high variability in results obtained on individual datasets. In practice, this would mean that this method would be less reliable, especially when working on a single set of image data—reliability would only increase with the analysis of multitemporal data. Therefore, the authors see a solution primarily in the introduction of additional radiometric correction of images, which would allow for the preparation of universal threshold values for indices, to be used in any area of Poland, and possibly even on data from different months. The correction method would have to be partially automated, for example, using unsupervised classifiers. Another possibility worth testing is the use of indices considered here as efficient (such as CBI, BAEI, BRBA, and even NBAI_G, NBAI_B), as additional data for image classification, which could raise the overall accuracy of excavation class recognition. The authors will continue research in both these directions. The ultimate goal is to develop an autonomous, largely automated system for monitoring illegal mining excavations.

Author Contributions: Conceptualization, K.M., E.G., T.P. and E.S.M.; Methodology, K.M., E.G., T.P. and E.S.M.; Validation, K.M., E.G., T.P. and B.S.; Investigation, K.M., E.G. and T.P.; Resources, K.M., E.G. and T.P.; Writing—original draft, E.G., T.P. and B.S.; Writing—review and editing, K.M., E.G., E.S.M., T.P. and B.S.; Visualization, E.G., T.P. and B.S.; Project administration, K.M. and E.G.; Funding acquisition, K.M. and E.G. All authors have read and agreed to the published version of the manuscript.

Funding: The project is implemented as part of the National Centre for Research and Development, Fast Track, contract no. POIR.01.01.01-00-1465/20-00. Co-financed by the European Union from the funds of the European Regional Development Fund under the Operational Programme Smart Growth.

Data Availability Statement: The data is unavailable due to privacy or ethical restrictions.

Conflicts of Interest: The authors declare no conflicts of interest.

References

1. Higher Mining Authority, Activities of Mining Offices in 2015–2022 Related to the Determination of the Increased Fee in Connection with the Conduct of Illegal Mining Operations. Available online: https://www.wug.gov.pl/o_nas/Dzialalnosc__okregowych_urzedow_gorniczych (accessed on 10 October 2023).
2. Richardson, A.J.; Wiegand, C.L. Distinguishing Vegetation from Soil Background Information. *Photogram. Eng. Remote Sens.* **1977**, *43*, 1541–1552.
3. Perry, C.R., Jr.; Lautenschlager, L.F. Functional equivalence of spectral vegetation indices. *Remote Sens. Environ.* **1984**, *14*, 169–182. [CrossRef]

4. Camalan, S.; Cui, K.; Pauca, V.P.; Alqahtani, S.; Silman, M.; Chan, R.; Plemmons, R.J.; Dethier, E.N.; Fernandez, L.E.; Lutz, D.A. Change Detection of Amazonian Alluvial Gold Mining Using Deep Learning and Sentinel-2 Imagery. *Remote Sens.* **2022**, *14*, 1746. [CrossRef]
5. Lobo, F.D.L.; Souza-Filho, P.W.M.; Novo, E.M.L.d.M.; Carlos, F.M.; Barbosa, C.C.F. Mapping Mining Areas in the Brazilian Amazon Using MSI/Sentinel-2 Imagery. *Remote Sens.* **2018**, *10*, 1178. [CrossRef]
6. Huete, A.R. A soil-adjusted vegetation index (SAVI). *Remote Sens. Environ.* **1988**, *25*, 295–309. [CrossRef]
7. Baret, F.; Guyot, G.; Major, D.J. TSAVI: A Vegetation Index Which Minimizes Soil Brightness Effects on LAI and APAR Estimation. In Proceedings of the 12th Canadian Symposium on Remote Sensing Geoscience and Remote Sensing Symposium, Vancouver, BC, Canada, 10–14 July 1989; pp. 1355–1358. [CrossRef]
8. Drury, S. *Image Interpretation in Geology*; Allen and Unwin: London, UK, 1987; p. 243.
9. Chen, W.; Liu, L.; Zhang, C.; Wang, J.; Wang, J.; Pan, Y. Monitoring the seasonal bare soil areas in Beijing using multi-temporal TM images. In Proceedings of the IEEE International Geoscience and Remote Sensing Symposium, Anchorage, AK, USA, 20–24 September 2004; Volume 5, pp. 3379–3382. [CrossRef]
10. Diek, S.; Fornallaz, F.; Schaepman, M.E.; De Jong, R. Barest Pixel Composite for Agricultural Areas Using Landsat Time Series. *Remote Sens.* **2017**, *9*, 1245. [CrossRef]
11. Deng, C.; Wu, C. BCI: A biophysical composition index for remote sensing of urban environments. *Remote Sens. Environ.* **2012**, *127*, 247–259. [CrossRef]
12. Deng, Y.; Wu, C.; Li, M.; Chen, R. RNDSI: A ratio normalized difference soil index for remote sensing of urban/suburban environments. *Int. J. Appl. Earth Obs. Geoinf.* **2015**, *39*, 40–48. [CrossRef]
13. Faridatul, M.I.; Wu, B. Automatic Classification of Major Urban Land Covers Based on Novel Spectral Indices. *ISPRS Int. J. Geo-Inf.* **2018**, *7*, 453. [CrossRef]
14. Nguyen, C.T.; Chidthaisong, A.; Kieu Diem, P.; Huo, L.-Z. A Modified Bare Soil Index to Identify Bare Land Features during Agricultural Fallow-Period in Southeast Asia Using Landsat 8. *Land* **2021**, *10*, 231. [CrossRef]
15. Lenarčič, A.Š. Multitemporal Land Cover Classification of Optical Satellite Imagery (in Slovenian). Ph.D. Thesis, University of Ljubljana, Ljubljana, Slovenia, 2018. Available online: https://repozitorij.uni-lj.si/Dokument.php?id=114214&lang=slv (accessed on 1 November 2023).
16. Rasul, A.; Balzter, H.; Ibrahim, G.R.F.; Hameed, H.M.; Wheeler, J.; Adamu, B.; Ibrahim, S.; Najmaddin, P.M. Applying Built-Up and Bare-Soil Indices from Landsat 8 to Cities in Dry Climates. *Land* **2018**, *7*, 81. [CrossRef]
17. Kawamura, M.; Jayamana, S.; Tsujiko, Y. Relation between social and environmental conditions in Colombo Sri Lanka and the urban index estimated by satellite remote sensing data. *Int. Arch. Photogramm. Remote Sens.* **1996**, *31*, 321–326.
18. Deventer, A.; Ward, A.D.; Gowda, P.H.; Lyon, J.G. Using thematic mapper data to identify contrasting soil plains and tillage practices. *Photogramm. Eng. Remote Sens.* **1997**, *63*, 87–93.
19. Zha, Y.; Gao, J.; Ni, S. Use of Normalized Difference Built-Up Index in Automatically Mapping Urban Areas from TM Imagery. *Int. J. Remote Sens.* **2003**, *24*, 583–594. [CrossRef]
20. Lin, H.; Wang, J.; Liu, S.; Qu, Y.; Wan, H. Studies on urban areas extraction from Landsat TM images. In Proceedings of the Conference of IEEE: International Geo-science and Remote Sensing Symposium (IGARSS), Seoul, Republic of Korea, 25–29 July 2005; Volume 6, pp. 3826–3829. [CrossRef]
21. Bouzekri, S.; Lasbet, A.A.; Lachehab, A. A new spectral index for extraction of built-up area using Landsat-8 data. *J. Indian Soc. Remote Sens.* **2015**, *43*, 867–873. [CrossRef]
22. Sun, G.Y.; Chen, X.L.; Jia, X.P.; Yao, Y.J.; Wang, Z.J. Combinational build-up index (CBI) for effective impervious surface mapping in urban areas. *IEEE J. Sel. Top. Appl. Earth Obs. Remote Sens.* **2016**, *9*, 2081–2092. [CrossRef]
23. Kapil, A.; Pal, M. Comparison of Landsat 8 and Sentinel-2 data for accurate mapping of built-up area and bare soil. In Proceedings of the 38th Asian Conference on Remote Sensing, New Delhi, India, 23–27 October 2017.
24. Piyoosh, A.K.; Ghosh, S.K. Development of a modified bare soil and urban index for Landsat 8 satellite data. *Geocarto Int.* **2018**, *33*, 423–442. [CrossRef]
25. Bouhennache, R.; Bouden, T.; Taleb-Ahmed, A.; Cheddad, A. A new spectral index for the extraction of built-up land features from Landsat 8 satellite imagery. *Geocarto Int.* **2018**, *34*, 1531–1551. [CrossRef]
26. Waqar, M.M.; Mirza, J.F.; Mumtaz, R.; Hussain, E. Development of New Indices for Extraction of Built-Up Area and Bare Soil. *Open Access Sci. Rep.* **2012**, *1*, 4.
27. Rogers, A.S.; Kearney, M.S. Reducing signature variability in unmixing coastal marsh Thematic Mapper scenes using spectral indices. *Int. J. Remote Sens.* **2004**, *25*, 2317–2335. [CrossRef]
28. Stathakis, D.; Perakis, K.; Savin, I. Efficient segmentation of urban areas by the VIBI. *Int. J. Remote Sens.* **2012**, *33*, 6361–6377. [CrossRef]
29. Zhou, Y.; Yang, G.; Wang, S.; Wang, L.; Wang, F. A new index for mapping built-up and bare land areas from Landsat-8 OLI data. *Remote Sens. Lett.* **2014**, *5*, 862–871. [CrossRef]
30. Zhao, H.; Chen, H. Use of Normalized Difference Bareness Index in Quickly Mapping Bare Areas from TM/ETM+. In Proceedings of the Geoscience and Remote Sensing Symposium, 2005 IEEE International Geoscience and Remote Sensing Symposium, 2005. IGARSS '05., Seoul, Republic of Korea, 29 July 2005; Volume 3. [CrossRef]
31. Xu, H. A new index for delineating built-up land features in satellite imagery. *Int. J. Remote Sens.* **2008**, *29*, 4269–4276. [CrossRef]

32. As-syakur, A.R.; Adnyana, I.W.S.; Arthana, I.W.; Nuarsa, I.W. Enhanced built-Up and bareness index (EBBI) for mapping built-up and bare land in an urban area. *Remote Sens.* **2012**, *4*, 2957–2970. [CrossRef]
33. Bhatti, S.S.; Tripathi, N.K. Built-up area extraction using Landsat 8 OLI imagery. *GIScience Remote Sens.* **2014**, *51*, 445–467. [CrossRef]
34. Li, H.; Wang, C.; Zhong, C.; Su, A.; Xiong, C.; Wang, J.; Liu, J. Mapping urban bare land automatically from Landsat imagery with a simple index. *Remote Sens.* **2017**, *9*, 249. [CrossRef]
35. Gautam, V.K.; Murugan, P.; Annadurai, M. A New Three Band Index for Identifying Urban Areas using Satellite Images. In Proceedings of the Global Civil Engineering Challanges in Sustainable Development and Climate Change [ICGCSC-17], Moodbidri, India, 17–18 March 2017.
36. He, C.; Shi, P.; Xie, D.; Zhao, Y. Improving the normalized difference built-up index to map urban built-up areas using a semiautomatic segmentation approach. *Remote Sens. Lett.* **2010**, *1*, 213–221. [CrossRef]
37. Azizi, Z.; Najafi, A.; Sohrabi, H. Forest canopy density estimating, using satellite images. In Proceedings of the 21st ISPRS Congress, Commission VIII, Beijing, China, 3–11 July 2008; Chen, J., Jiang, J., Peled, A., Eds.; pp. 1127–1130.
38. Abdollahnejad, A.; Panagiotidis, D.; Surový, P. Forest canopy density assessment using different approaches—Review. *J. For. Sci.* **2017**, *63*, 107–116. [CrossRef]
39. Akike, S.; Samanta, S. Land Use/Land Cover and Forest Canopy Density Monitoring of Wafi-Golpu Project Area, Papua New Guinea. *J. Geosci. Environ. Prot.* **2016**, *4*, 1. [CrossRef]
40. Rouibah, K.; Belabbas, M. Applying Multi-Index approach from Sentinel-2 Imagery to Extract Urban Area in dry season (Semi-Arid Land in North East Algeria). *Rev. Teledetección* **2020**, *56*, 89–101. [CrossRef]
41. Daryl, M.; Janiola, C.; Pelayo, J.L.; Gacad, J.L.J. *Distinguishing Urban Built-Up and Bare Soil Features from Landsat 8 OLI Imagery Using Different Developed Band Indices*; Central Mindanao University: Bukidnon, Philippines, 2015.
42. Sekandari, M.; Masoumi, I.; Pour, B.A.; Muslim, M.A.; Rahmani, O.; Hashim, M.; Zoheir, B.; Pradhan, B.; Misra, A.; Aminpour, S.M. Application of Landsat-8, Sentinel-2, ASTER and WorldView-3 Spectral Imagery for Exploration of Carbonate-Hosted Pb-Zn Deposits in the Central Iranian Terrane (CIT). *Remote Sens.* **2020**, *12*, 1239. [CrossRef]
43. Stančič, L.; Oštir, K.; Kokalj, Ž. Fluvial gravel bar mapping with spectral signal mixture analysis. *Eur. J. Remote Sens.* **2021**, *54*, 31–46. [CrossRef]
44. Kruse, F.A.; Lefkoff, A.B.; Boardman, J.W.; Heidebrecht, K.B.; Shapiro, A.T.; Barloon, P.J.; Goetz, A.F.H. The Spectral Image Processing System (SIPS)—Interactive Visualization and Analysis of Imaging Spectrometer Data. *Remote Sens. Environ.* **1993**, *44*, 145–163. [CrossRef]
45. Usmanov, B.M.; Isakova, L.S.; Mukharamova, S.S.; Akhmetzyanova, L.G.; Kuritsin, I.N. Automated detection of illegal nonmetallic minerals mining places according to Sentinel-2 data. In Proceedings of the Earth Resources and Environmental Remote Sensing/GIS Applications XII, 118631C, Online, 12 September 2021; Volume 11863. [CrossRef]
46. Kondracki, J. *Geografia Regionalna Polski*; PWN: Warszawa, Poland, 2001; p. 441.
47. Richling, A.; Solon, J.; Macias, A.; Balon, J.; Borzyszkowski, J.; Kistowski, M. (Eds.) *Regionalna Geografia Fizyczna Polski*; Bogucki Wyd. Naukowe: Poznań, Poland, 2021; p. 608.
48. Corine Land Cover 2018 (CLC2018). Institute of Geodesy and Cartography, Chief Inspectorate for Environmental Protection. Available online: https://clc.gios.gov.pl/index.php/clc-2018/udostepnianie (accessed on 14 October 2023).
49. ESA (European Space Agency). 2023. Available online: https://scihub.copernicus.eu/ (accessed on 10 March 2023).
50. QGIS Development Team. QGIS Geographic Information System, v. 3.23; Open Source Geospatial Foundation Project. 2023. Available online: http://qgis.osgeo.org (accessed on 10 October 2023).
51. PIG (Polish Geological Institute), MIDAS Database. 2023. Available online: https://baza.pgi.gov.pl/geoportal/uslugi/gis (accessed on 10 March 2023).
52. Radeloff, V.C.; Mladenoff, D.J.; Boyce, M.S. Detecting Jack Pine Budworm Defoliation Using Spectral Mixture Analysis. *Remote Sens. Environ.* **1999**, *69*, 156–169. [CrossRef]
53. Su, S.; Tian, J.; Dong, X.; Tian, Q.; Wang, N.; Xi, Y. An Impervious Surface Spectral Index on Multispectral Imagery Using Visible and Near-Infrared Bands. *Remote Sens.* **2022**, *14*, 3391. [CrossRef]
54. Olofsson, P.; Foody, G.M.; Herold, M.; Stehman, S.V.; Woodcock, C.E.; Wulder, M.A. Good Practices for Assessing Accuracy and Estimating Area of Land Change. *Remote Sens. Environ.* **2014**, *148*, 42–57. [CrossRef]
55. Foody, G.M. Status of land cover classification accuracy assessment. *Remote Sens. Environ.* **2002**, *80*, 185–201. [CrossRef]
56. Du, Y.; Zhang, Y.; Ling, F.; Wang, Q.; Li, W.; Li, X. Water Bodies' Mapping from Sentinel-2 Imagery with Modified Normalized Difference Water Index at 10-m Spatial Resolution Produced by Sharpening the SWIR Band. *Remote Sens.* **2016**, *8*, 354. [CrossRef]
57. Chen, J.Y.; Yang, K.; Chen, S.Z.; Yang, C.; Zhang, S.H.; He, L. Enhanced normalized difference index for impervious surface area estimation at the plateau basin scale. *J. Appl. Remote Sens.* **2019**, *13*, 016502. [CrossRef]
58. Liu, Y.-L.; Yin, H.-D.; Xiao, T.; Huang, L.; Cheng, Y.-M. Dynamic Prediction of Landslide Life Expectancy Using Ensemble System Incorporating Classical Prediction Models and Machine Learning. *Geosci. Front.* **2024**, *15*, 101758. [CrossRef]
59. Digra, M.; Dhir, R.; Sharma, N. Land use land cover classification of remote sensing images based on the deep learning approaches: A statistical analysis and review. *Arab. J. Geosci.* **2022**, *15*, 1003. [CrossRef]
60. Carranza-García, M.; García-Gutiérrez, J.; Riquelme, J.C. A Framework for Evaluating Land Use and Land Cover Classification Using Convolutional Neural Networks. *Remote Sens.* **2019**, *11*, 274. [CrossRef]

61. Robinson, Y.H.; Vimal, S.; Khari, M.; Hernández, F.C.L.; Crespo, R.G. Tree-based convolutional neural networks for object classification in segmented satellite images. *Int. J. High Perform. Comput. Appl.* **2020**, 1–14. [CrossRef]
62. Tahir, A.; Munawar, H.S.; Akram, J.; Adil, M.; Ali, S.; Kouzani, A.Z.; Mahmud, M.A.P. Automatic Target Detection from Satellite Imagery Using Machine Learning. *Sensors* **2022**, *22*, 1147. [CrossRef] [PubMed]